Short Wavelength a-Si:H Photodetector for Bio-molecular Fragment Sizing

by

Ida Khodami

A thesis
presented to the University of Waterloo
in fulfillment of the
thesis requirement for the degree of
Master of Applied Science
in
Electrical and Computer Engineering

Waterloo, Ontario, Canada, 2007

I hereby declare that I am the sole author of this thesis. This is a true copy of the thesis, including any required final revisions, as accepted by my examiners.

I understand that my thesis may be made electronically available to the public.

Abstract

A gel electrophoresis technology based on absorption of ultraviolet radiation for fragment sizing of bio-molecular segments such as protein and nucleic acid is introduced for the first time. The new technology has the potential to improve conventional gel electrophoresis method by lowering the cost and increasing the throughpxcvfut. A cost effective, high sensitivity, short wavelength selective detector is an essential component to enable the proposed technology. In this thesis, hydrogenated amorphous silicon (a-Si:H) metal semiconductor metal(MSM) are investigated as the short wavelength detector of choice. The operation of planar MSM photoconductor-based photo detectors with very thin a-Si:H film thickness and aluminium electrodes is investigated. Experimental results of photocurrent measurements as well as responsivity and quantum efficiency are presented. The MSM photodetectors presented are fully compatible with state-of-the-art staggered gate thin film transistor (TFT) fabrication processes to enable large area pixel arrays for bio-molecular imaging.

Acknowledgement

I would first like to express my gratitude to my senior supervisor, Dr. Karim S. Karim, for his continual support and guidance that have allowed my dreams and ideas to come to existence; without his instructive comments and encouragement this thesis work would not have been possible. Second, I would like to thank every member of the Silicon Thin-film Applied Research (STAR) group, who has supported me throughout my years in the program, all my friends especially Mr. Farahad Taghibakhsh and Mr. Amir Goldan. Special thanks to Mr. Farahad Taghibakhsh for valuable technical discussion and assistant in the final stages of this thesis, also from STAR group: thanks to Dr. Xinyo Wang, and Miss Wing Fai Lydia Tse for trusting me with her final samples for XRD and TEM testing.

The following people from the Department of Physics at Simon Fraser University have also assisted with performing numerous material characterizations: Dr. Karen Kavanagh for her guidance especially in improving the a-Si:H p^+ layer, and Dr. Li Yang for Transmission Electron Microscopy; Also especial thanks to Mr. Edward Leung for great discussions regarding molecular biology and biochemistry matters and all the help with preparation of the electrophoresis testing.

In addition, I would like to show my appreciation to the following organizations for funding my research: National Sciences and Engineering Research Council of Canada (NSERC), Canada Foundation of Innovation (CFI), British Columbia Knowledge Development Fund (BCKDF), Simon Fraser University (SFU), and finally University of Waterloo (UW).

I would like to express 100% gratefulness to my family for their endless love and support. Without the time and effort that my parents, Nasrin Hojjati and Mansour Khodami, spent in raising me, I would not have been able to get to where I am. Sincere thanks to my adorable sister, Pantea, for her many encouraging comments and love that have helped me live through all stressful times and have let me see the bright side whenever I wasn't able to.

CONTENTS

List of Table

List of Figures

1 Chapter 1: Introduction

1.1 Short wavelength detectors

Ultraviolet research began in the latter half of the 19^{th} century, when the invisible radiation beyond the blue end of the visible spectrum began to receive attention. Ultra violet (UV) spectrum is separated in to three parts, UV-C (200-280nm), UV-B (280-320nm), and UV-A (320-400nm). UV detection has many applications in civil, military and biomedical technologies; such as chemical and biological analysis (ozone, pollutants, and most organic compounds present absorption lines in the UV spectral range), flame detection(including fire alarm, missile warning or combustion monitoring), optical communications(particularly inter satellite communications at $\lambda<280$nm) emitter calibration (instrumentation, UV lithography), astronomical studied, [1] and detection of the variation of DNA absorbance of UV with specific application to genome projects [2]. In this research we are focusing on the latter application mainly for genome projects.

Short wavelength detectors can be classified into three main types:

(1) Thermal detectors: thermopiles and pyroelectric detectors;

(2) Photomultiplier tubs (PMT);

(3) Semiconductor photo detectors.

In thermal detectors, the incident radiation is absorbed and upon this absorption the temperature of the material rises up; one disadvantage of these detectors is that thermal effects are wavelength independent. Therefore thermal detectors are not the best choice where high sensitivity and high selectivity are required.

Another alternative that has been used for many decades as the main UV detector are photomultiplier tubes (PMT). PMTs have the advantage of high sensitivity and selectivity to UV. However, these detectors are fragile, bulky, need large power sources and are expensive.

For biomedical applications, the main focus of this study, special requirements and challenges for detectors are introduced, and continuous development for obtaining better performance and lower cost detectors are pursued. Semiconductor detectors have much lower cost compared to PMTs, and show a selective wavelength dependence of the response per unit incident radiation power compared to thermal detectors. Semiconductor photodetectors require moderate biases, are small, lightweight, and have fairly high sensitivity to UV light which makes them a good approach for UV detection. The properties of the above different short wavelength detectors without any amplification are summarized in Table 1 [3].

Table 1: Comparing properties of ultraviolet detectors without any amplification.

Type	QE	RESPONSIVITY	FILTERING	SIZE
Thermal	Low	Low	Extensive	Small
Photomultiplier tubes	Low-Medium	Very High	Variable	Large
Semiconductor photo detectors	Medium-High	Medium-High	Variable	Small

Within semiconductor photo detectors, crystalline silicon (c-Si) CCD devices are one option for UV detection [4]. However for large area applications hydrogenated amorphous silicon (a-Si:H) are lower in cost and have better sensitivity to shorter wavelength compared to c-Si. In this research hydrogenated amorphous silicon (a-Si:H) detector for short wavelength detection is discussed.

1.2 Hydrogenated Amorphous Silicon Technology

Silicon (Si) is the second most abundant element on earth which has a much lower material cost compared to other semiconductors such as Germanium (Ge). While crystalline silicon (c-Si) offers advantages over other expensive semiconductors, its production costs are high in large area applications, as a result, hydrogenated amorphous silicon (a-Si:H) technology with lower production costs is dominant.

Crystalline silicon atoms form four tetrahedral oriented covalent bonds with four adjacent neighbors which means they have long range ordered structure, but a-Si:H lacks the periodicity and long range order. Therefore a-Si:H only share properties based on short range bonding interaction with c-Si. Nevertheless, the material properties of a-Si are significantly different from those of c-Si. For example, the optical band gap increases from 1.1 eV in crystalline silicon to 1.7 eV in amorphous silicon and the absorption coefficient of a-Si for shorter wavelength is higher than that of crystalline silicon. This higher band gap makes a-Si:H a better candidate for short wavelength detection.

a-Si:H technology is the basis of a multi-billion dollar market in diverse applications such as active matrix liquid crystal displays (AMLCD), electro-photography, image sensors, and solar cells [5]. These devices result from properties of a-Si:H material such as high photosensitivity, reasonably short response time, combined with specifics of a-Si:H technology such as the capability for large area fabrication, low temperature processing and high production yield [5].

1.3 Hydrogenated Amorphous Silicon Photodetectors

Image sensors fabricated using a-Si:H as photosensitive semiconductor commercialized to date can be divided into two main types depending on the direction of incident light and with respect to the applied field, i.e. photoconductive (PC) and photovoltaic (PV) type detectors[6]. In PC detectors the coplanar structure of the detector allows the incident light to be perpendicular to the applied electric field and photocurrent flow is in a horizontal direction between the electrodes, where as in PV detectors light is incident parallel to the applied electric field and the semiconductor layer is sandwiched between the two electrodes and photocurrent is in a vertical direction between the top and bottom electrode (Figure 1).

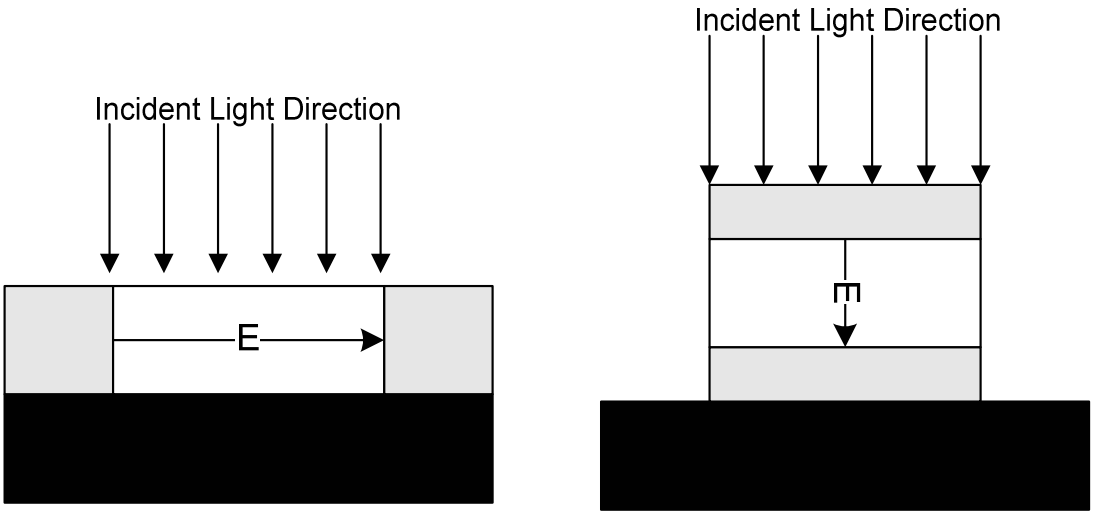

Figure 1: Structures of photoconductive (PC) left, and photovoltaic type (PV) right sensors.

In PC detectors the semiconductor is directly exposed to illumination and detection is carried out upon modulation of the resistivity of the active layer when a constant voltage is applied between metal electrodes. On the other hand the PV detectors are diode like detectors and are operated with a reverse bias. The most common a-Si:H PV are p-i-n diode structures (i.e. a stacked structure consisting of p^+ a-Si:H, i-a-Si:H and n^+ a-Si:H films with electrical contacts on either side) mainly because the depletion width thickness in the intrinsic layer can be tailored to

optimize quantum efficiency of detection. Due to the high defect density in the doped layer in amorphous silicon detectors, three layers exist instead of two. p and n layers create the built-in voltage, and will not contribute to charge collection, and all the charge collections take place in the intrinsic a-Si:H layer. A detailed discussion of these detectors appears in a later chapter.

1.4 Photodetectors Figure of merit

Depending on the application some design parameters in the detector carry more weight than the others. However, in designing any photodetector there are some common parameters that define the quality of the detector: spectral responsivity, signal-to-noise (photoresponse), External quantum efficiency (EQE), selectivity (filtering requirements), signal linearity with respect to optical power, and size of the detector. An introductory definition of each of these parameters is given as follows.

- *Spectral Responsivity*

Spectral Responsivity (R) with units of A/W measures the photo induced signal of detector I_{ph} which is (I_{illum} -I_{dark}) compared to the incident optical power P_{inc} from the illuminating source.

$$R = \frac{I_{Ph}}{P_{inc}} = \frac{I_{illum} - I_{dark}}{P_{inc}} \qquad \textbf{Equation 1}$$

- *Photo-response*

Photo-response which is a unit less ratio compares the illumination current I_{illum} to dark current I_{dark}.

$$R_{L/D} = \frac{I_{illum}}{I_{dark}} \qquad \textbf{Equation 2}$$

- *External quantum efficiency (EQE)*

EQE is usually reported in percentage form (%) and shows the overall performance of photodetectors. EQE is defined to be the ratio of charge flux to photon flux, demonstrating how effectively the incident photon flux is converted to charge carriers, and how effectively those carriers are collected.

$$EQE = \frac{I_{ph} / q}{P_{inc} / h\nu} \qquad \textbf{Equation 3}$$

- *Filtering requirement*

In order to use a short wavelength detector in any test condition, either a filtering system should be applied to filter the ambient light or the detector has to be visible blind which blocks the ambient light with out requiring a filtering system.

- *Signal linearity with respect to optical power*:

Linear detectors enable the user to use the detector with different optical power and be able to predict the output signal, which is beneficial in applications where different optical power needs to be used.

- *Size and cost*

Size and cost are two closely connected parameters. The fabrication cost in terms of photolithography, number of masks required, etc of the detector for very small detectors in a large area imager where many of such detectors are needed is an important parameter when comparing different detectors to choose the best quality detector.

1.5 Thesis outline

This dissertation is organized into four main areas: Background, Motivation of work, Metal Semiconductor Metal (MSM) results and finally the conclusion and future work. The first part, which includes chapter 1 provides a general background on short wavelength a-Si:H detectors. Chapter 2 presents a new and novel application for bio-molecular fragment sizing, followed by a first prototype developed using off-the-shelf components. Chapter 3 starts by introduction on prior art and follows by an initial implementation and results obtained for in-house fabricated MSM a-Si:H structures. A good understanding of background is important, and chapter 1 aims at providing the necessary background material related to this topic. Building on the ground work from the first chapter, chapter 2 introduces the novel application and specific requirements for this novel application that has to be met with the detector design. And finally the last chapter examines the new MSM thin film design and present the characteristics of this photoconductor. The fabricated device and the test results are all described in this third chapter. The last section concludes the thesis with a summary of the project and presents a path to be pursued for further research in this area.

2 Chapter 2: A novel method for bio-molecular fragment sizing

2.1 Introduction to DNA and Bio-molecular imaging applications

Deoxyribonucleic acid (DNA) is a nucleic acid that contains the genetic information for the development and function of living organisms. The information attained from genetic DNA analysis can revolutionize the diagnosis, prevention and treatment of many human diseases such as cancer, cardiovascular, and Alzheimer's. DNA analysis is rapidly making the transition from a purely scientific quest for accuracy to a routine procedure with increased proven dependability. Most DNA fragment analysis used in laboratories is performed using a slab gel-based electrophoresis, which has been routinely used since its inception more than 20 years ago. The term electrophoresis refers to the movement of a charged molecule under the influence of an electric field. Electrophoresis can be used to separate molecules that have equivalent charge-to-mass ratios but different masses. One such type is a multi-lane slab gel electrophoresis instrument, which uses a slab of Agarose gel with some introduced channels using a comb on which DNA samples are placed. An electric voltage is applied across the gel slab, generating a field that separates the DNA sample into fragments of different masses (fragment sizing) [7], [8], and [9]. DNA fragments in gel slab method are conventionally detected by directing light at the components separating from the sample, where each component (or fragment) has been previously tagged with a fluorescent dye. Detecting the fluorescence emissions induced by this incident light is important. The primary challenge relates to sample detection techniques with fluorescence staining. Usually the users need to stain the gel with the fluorescence dye before

imaging and then use scanners to perform the DNA analysis. The tedious and cumbersome fluorescence staining method is not suited for a high-throughput and low cost DNA analysis application. In order for DNA fragment analyzing instrumentation to be competitive on a throughput basis, it is necessary to develop instruments that can run many samples at a time. Also to simplify the method, eliminating the fragment staining step is ideal.

Conventional gel electrophoresis for DNA analysis is labor-intensive and does not exhibit high resolving power or throughput, but is still routinely used by medical researchers, pharmacologists, and forensic investigators for want of a better method. To address the need for a technology that is more sensitive, high-throughput, less labor intensive and cost effective, we propose the alternative novel method for bio-molecular fragment sizing described below.

2.2 Introducing the Novel method of bio-molecular fragment sizing

In conventional gel electrophoresis, the bio-molecules in a gel support are separated by an electric field. Negatively charged molecules move toward the anode side of the gel, and positively charged molecules move toward the cathode side. For example, DNA by nature has a negative charge so upon applying electric field the DNA fragments start moving towards the cathode side.

The channels are created inside the gel by placing a comb in the gel (from this point on we will refer to these channels as “separating channels”. The comb makes wells of a predetermined size in the gel. Then, the DNA strand that is previously cut into smaller fragments using DNA endonuclease enzyme is loaded in the separating channels of the gel and allowed to separate for some time via the electric field that forces the fragments to migrate through the gel. DNA molecules migrate from negative to positive potential due to the net negative charge of the

phosphate backbone of the DNA chain. When the separation is completed, the fragments are visualized by using a fluorescent dye (labeling method) specific for DNA. Fragment size determination is typically done by comparison to commercially available DNA ladders (i.e. the control) containing linear DNA fragments of known length. The moving speed of the loaded sample depends on their properties. There are many factors that determine the moving rate of these molecules through the meshwork: the electric field's strength, the gel support or matrix composition, the liquid buffer solution's composition, the molecules' size, shape and charge, and chemical composition of the molecules being separated. The smaller molecules move faster than larger molecules because they encounter less frictional drag in the gel.

Traditionally, DNA fragment sizing is done by using a fluorescent dye labeling. We propose a label-free fragment sizing of bio-molecular fragments based on the absorption variation of UV radiation through the DNA. The technique relies implicitly on the knowledge that DNA and proteins absorb UV radiation. For example, DNA absorbs strongly at 260 nm wavelength [2] (see Figure 2) and proteins are known to absorb highly at 280 nm.

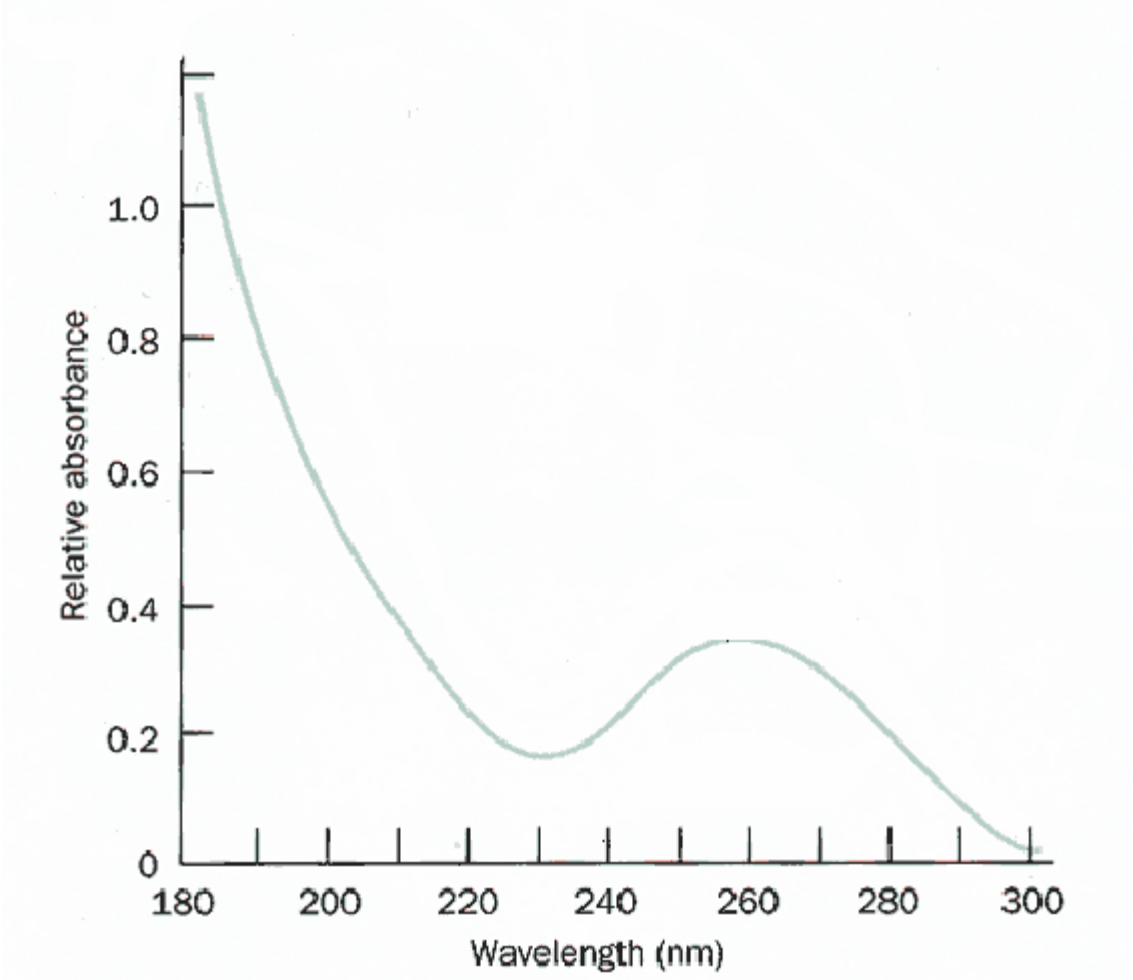

Figure 2: Relative absorbance spectrum of double strand DNA.

The proposed method consists of a linear array of UV sensitive detectors, and a source of low intensity monochromatic UV light (for example for DNA fragment sizing, the light source has to be 260nm). In order for DNA fragment analyzing instrumentation to be competitive on a throughput basis, it is necessary to develop instruments that can run many samples at the same time. Therefore by using a linear array, the fragment sizing is done simultaneously in all separating channels in the electrophoresis gel. The detection region along each separation channel will define a detection zone for analytes where the source and the detector should be placed; the light source is located above the detection zone and the detector array is placed

underneath the detection zone. As analytes (for example DNA fragments) pass the detection zone in their defined separating channels, absorption of DNA at 260nm wavelength light will cause a reduction in the read out of detector signal. As will be explained in section 2.3.1, depending on the concentration of the Agarose gel used the readout signal from the detector might be slightly different each time the fragment sizing analysis is performed using the proposed method. In order to do a self calibration so that the proposed method does not depend on the gel concentration used, each time before starting the electrophoresis, the signal from the sensor with only the Agarose gel in the detection zone has to be read and saved; this will provide the amount of UV absorbed by the Agarose gel and the buffer solution alone and we call it A_{BUFFER}; then the electrophoresis begins and the detector signal is readout frequently. Each time the readout output is saved and compared to A_{BUFFER}. It should be noted that since DNA has highest absorption in 260nm wavelength, anytime an analyte is passing the detection zone A_n (if the analyte is DNA then $A_{DNA\ presence}$) Will be less than A_{BUFFER} Figure 3 provide a detailed flowchart of the above explained self calibration technique of the proposed method.

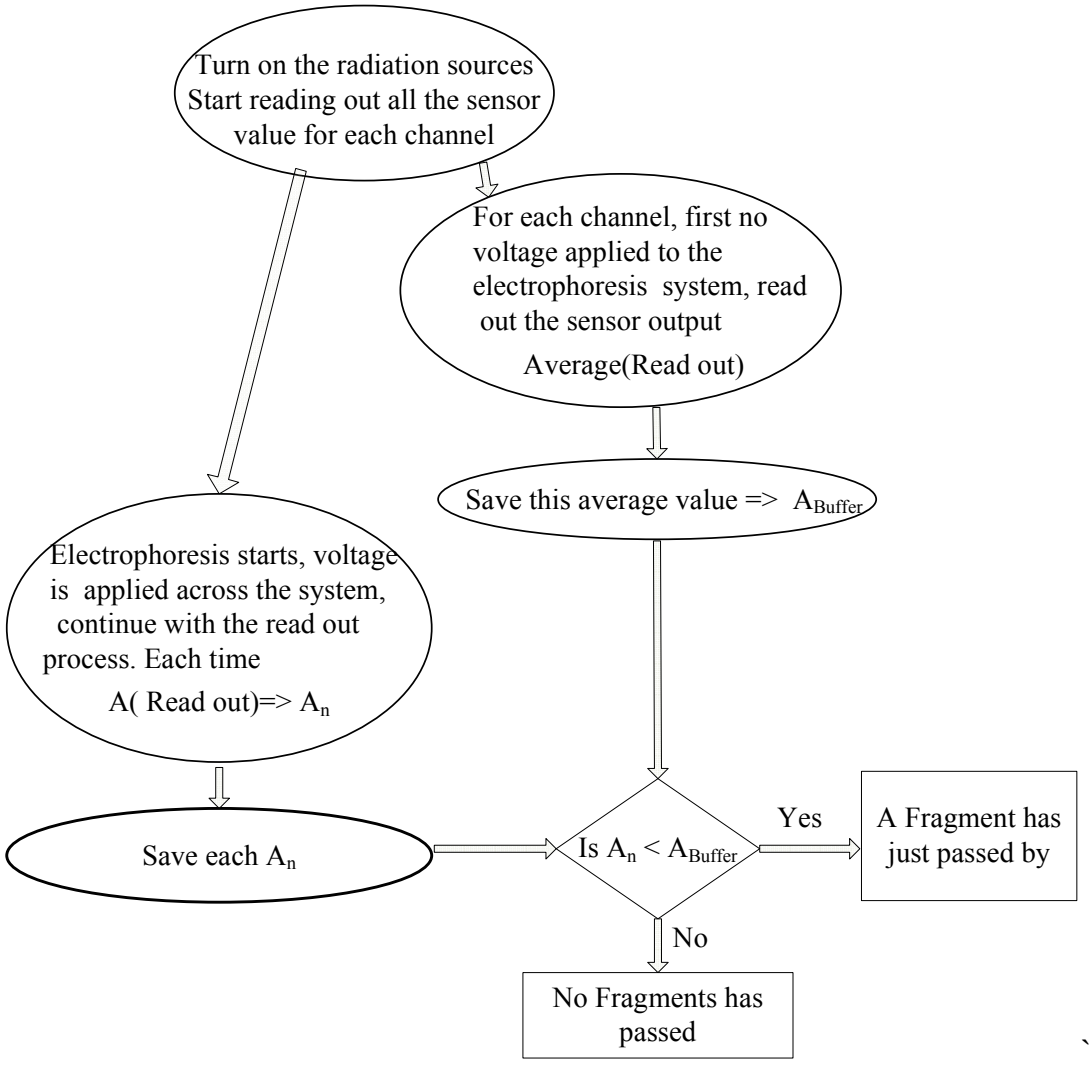

Figure 3: Flowchart description of the bio-separation device for fragment sizing.

By connecting the detector to a controller, the read out can be stored frequently as shown in the functional diagram in Figure 4 (a) and (b). A simple way to envision the proposed new technology is as if pictures of the movement of DNA fragments are taken. In the proposed method for DNA fragment sizing, a detection scheme that is faster, more sensitive, more accurate, and cheap is achievable.

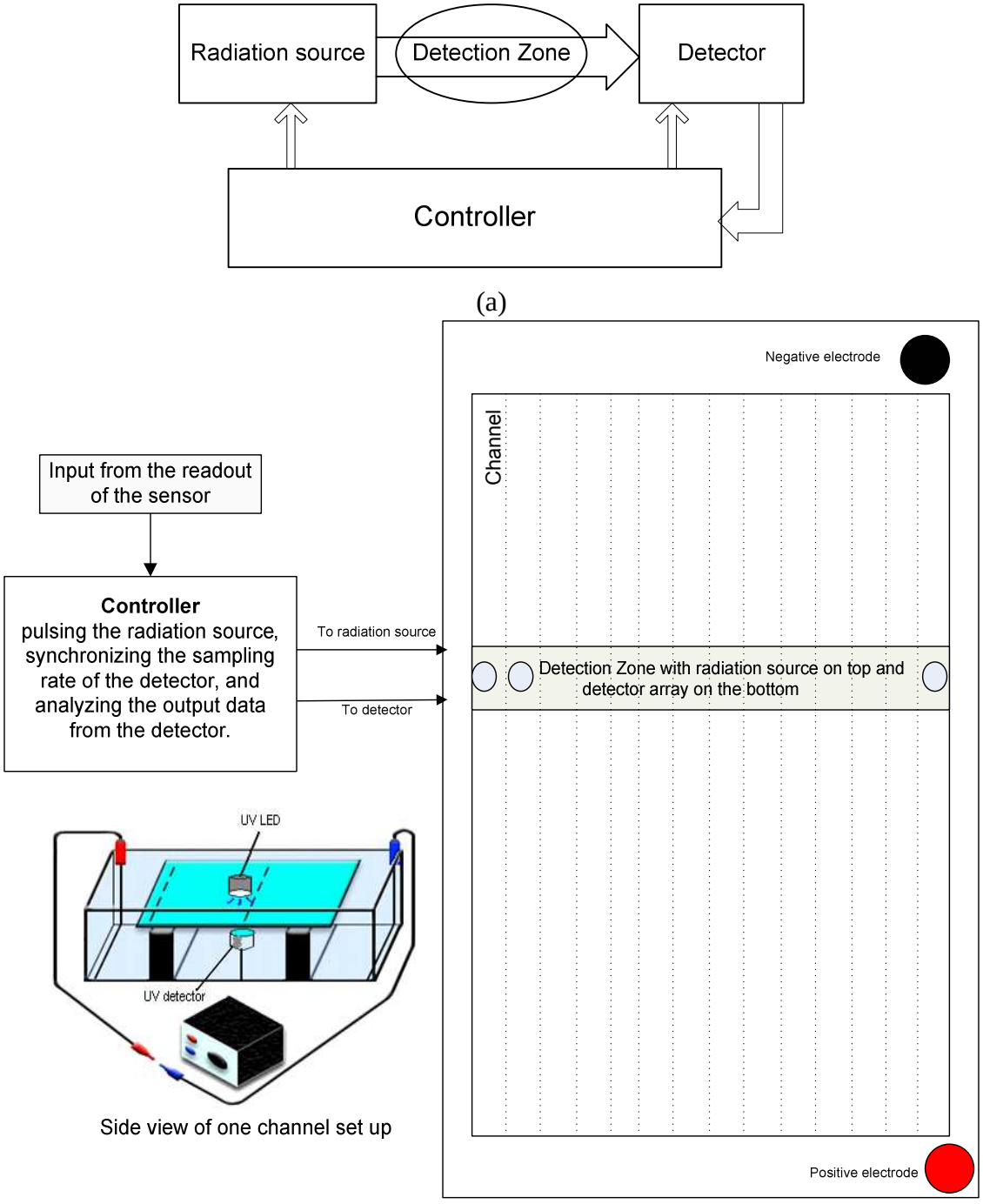

Figure 4: (a) Functional block diagram of the new bio-separation system components, and (b) perspective view of an example of gel-slab electrophoresis technology with one embodiment of the present invention.

The driving force for separation in slab gel electrophoresis is the Lorentz force. The Lorentz force is the force (Equation 4) exerted on a charged particle in an electromagnetic field and is affected by the ambient electrical conditions and the electrical properties of the particle that is under study.

$$F_{Lorentz} = q \times (E + v \times B)$$ **Equation 4**

Where F is the Lorentz force (in Newtons), E is the electric field (in volts/meter), B is the magnetic field (in Teslas), q is the electric charge of the particle (in Coulombs), and v is the instantaneous velocity of the particle (in meters/second). In electrophoresis analysis B is set to zero for simplification, then Lorentz force becomes coulomb's law:

$$F_{Lorentz} = q \times E$$ **Equation 5**

The resulting analytes migration due to Lorentz force is countered by friction such that the rate of migration is constant in a constant and homogenous electric field. Where the friction force is defined as:

$$F_{friction} = v \times f$$ **Equation 6**

Where f is the frictional coefficient in Equation 6. So now if the analyte is moving in the mesh like gel with a constant mobility, due to Newton's law of forces, the total force is equal to:

$$F = m \times a$$ **Equation 7**

Where m is the mass (in Kilograms) and a (in meters/second squared) is the acceleration. In gel electrophoresis the total forces are only the Friction force subtracted from the Lorentz force, and assuming constant velocity of analyte, the acceleration is zero. Therefore we have:

$$F_{Total} = F_{Lorentz} - F_{friction} = 0$$

or

Equation 8

$$q \times E = V \times f$$

Mobility is dependent on both the analyte properties and solution properties. Electrophoresis analytes mobility assuming a constant velocity of analyte is then defined as

$$\mu = \frac{V}{E} = \frac{q}{F}$$

Equation 9

The following is a simple calculation of how the proposed method works:

Imagine in a normal experiment that the length of the gel from anode to cathode is 30 cm and each separating channel well is 1mm. In a normal gel electrophoresis, the experimenter leaves the electrophoresis experiment to run for about 6 hours, which is roughly the amount it takes for the fastest analyte to migrate from the cathode to the anode. Therefore if it takes 6 hours to migrate 30 cm it should approximately take 1 hour (assuming linear mobility relation) to migrate 5 cm and 1second to migrate 14 μm about 0.072 second to migrate 1 μm for the fastest analyte, or 72 millisecond to migrate 1 μm. From these calculations if the readout is faster than 1 millisecond, resolution better than 1 μm for fragments sizing is achieved.

Another consideration is the size of the sensor or the width of each detector in the detector array; since the separating channel wells are 1 mm the sensor should be designed exactly 1 mm in width to gather maximum data regardless of where the analyte is exactly situated when moving

in the separation channel well in the detection zone. For example if we assume each separating channel well is divided in three sections, a, b, and c, by designing the sensor to cover the whole width of the separating channel well we ensure that no matter where the analyte is (a, b, or c) while moving along the detection zone it is still in the detection field of the detector.

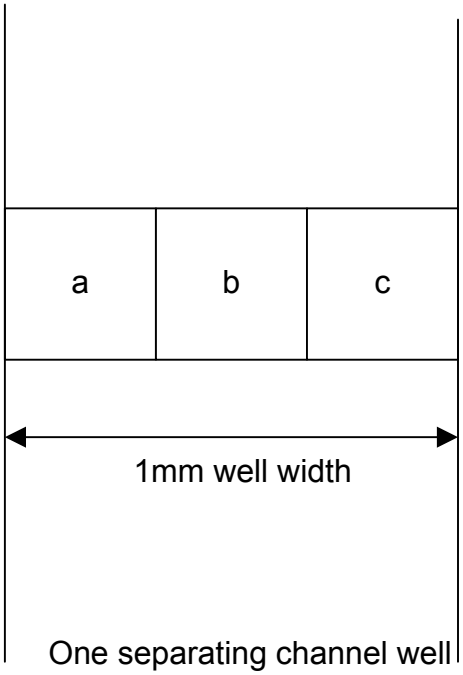

Figure 5: Determining the width of each detector in the sensor array.

Therefore the new proposed method provides a multi-channel detection scheme based on a multi-radiation source/linear array detector configuration, in which direct detection is conducted without staining the analytes. Each single detector in the array is coupled to a single radiation source. Bio-separation is conducted simultaneously in all the channels in parallel, the light sources direct radiation at the detection zones; the detector sampling rate is predefined and each time the sampled readout signal from the detector is saved in the controller for further analysis.

2.3 Proof of concept of the novel method of bio-molecular fragment sizing

This section presents detail of the initial work that was done to demonstrate the feasibility of the proposed method. At the end of this chapter the specific requirements for the a-Si:H UV detector array for bio-molecular fragment sizing are specified. This section includes four segments. The first segment test the absorption of Agarose gel to examine if the same medium as the conventional method for electrophoresis analysis can be used in the new proposed method.

The second section specify the requirement of the off the shelve components that were used; the third section specifies the improvement that were done on the conventional gel box for the proposed new electrophoresis analysis and finally the last part will demonstrate the obtained feasibility testing results.

2.3.1 Agarose Gel UV absorption

The amount of absorption of Agarose gel at 260nm is important because Agarose gel is the medium that the DNA's are loaded in. Therefore we first tested the Agarose gel with three different concentrations and same thickness to find the transmittance of UV through the gels. Three samples of Agarose gel made for electrophoresis analysis with different concentration were tested under UV-Visible spectroscopy. In this test, the results of the tests demonstrate negligible absorption for all three different concentrations of Agarose gel (Figure 6, Figure 7, and Figure 9). The highest absorption was observed for gel with highest concentration (1 %).

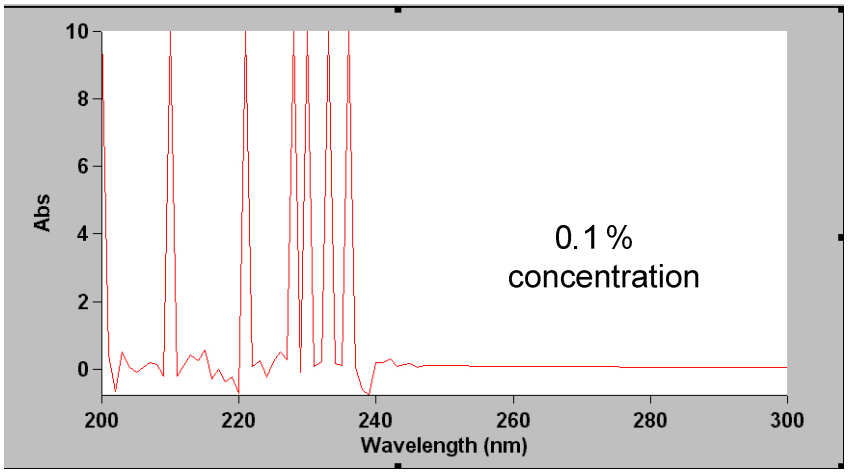

Figure 6: Absorbance spectrum of 0.5% Agarose gel in 1cm cuvette.

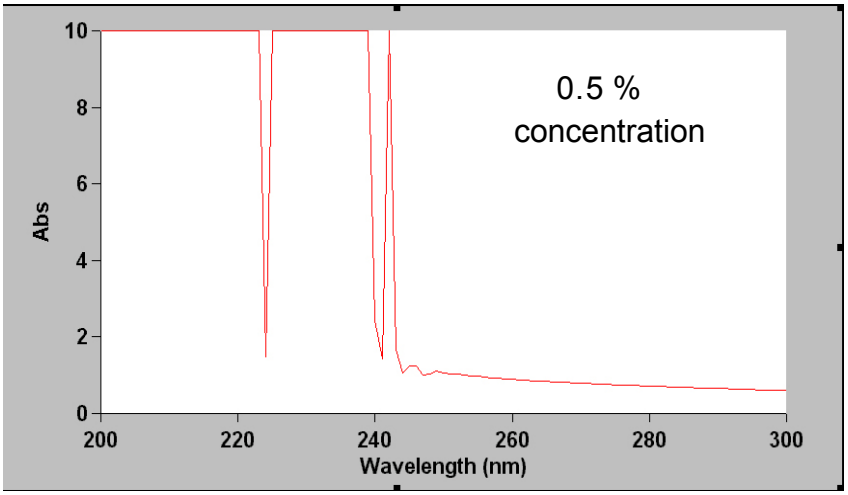

Figure 7: Absorbance spectrum of 0.5% Agarose gel in 1cm cuvette.

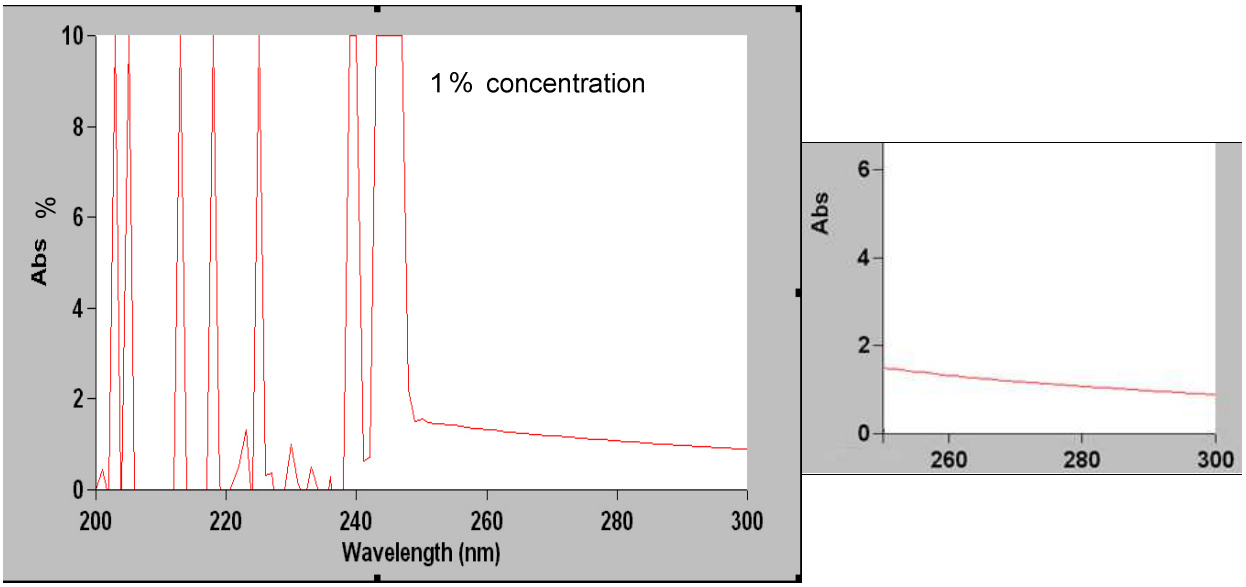

Figure 8 : Absorption spectrum of Agarose gel with concentrations of 1% (left) , zoom in on the absorption for wave length between 250-300nm (right).

Therefore, Agaorose gel can still be used as the medium for electrophoresis in the new proposed technology, since it does not block the transmittance of 260nm UV to the DNA fragments.

We chose off the shelf components as described in following sections to study the feasibility of using the UV absorption for DNA fragment sizing in gel electrophoresis. As mentioned before in the proposed method a source, a detector and a controller is required for each separating channel.

2.3.2 Source Requirements

The off the shelf UV light source must satisfy the following requirements:

1. The output wavelength must have maximum power at around 260nm. (With very narrow output spectrum).
2. The UV light source must be small, light and inexpensive.

3. The output beam must have a spot size around 1mm. Since the width of each separating channel is 1mm, a spot size of 1mm would match the channel width without spreading over to adjacent channels.

For the first prototype to show how feasible the idea is, a 265nm UV LED (UVTOP®) [10] was chosen as the UV light source for the test apparatus. Other options were UV gas lasers, UV laser diodes, and UV lamps. However, the best choice in terms of cost and low power was the UV laser diode with specifications listed in Table 2.

Table 2: Specifications of UVTOP ® UV LED

Maximum output power:	0.5 mW
Maximum wavelength:	265 nm
Spectrum range:	±12 nm
Spot size:	1.5 mm
Focal length:	14 mm
Size:	8 mm diameter
Maximum forward current:	30 mA
Forward voltage maximum:	7.5V at 20 mA

2.3.3 Detector Requirements

The off-the-shelf UV detector must satisfy following requirements:

1. Small enough to improve the detection resolution but wide enough to cover the hole width of the separating channel.

2. Small detection area, around 1mm^2. This will minimize the crosstalk between channels from adjacent sample channels for multi channel test set up.
3. High sensitivity and selectivity to 260 nm, and low sensitivity to ambient light.

For the first prototype, a UV photodiode detector (JIC168C) [11] with an integrated amplifier and externally adjustable gain was chosen (Table 3).

Table 3: JIC168C UV photo detector specifications.

Spectral range:	210 nm to 280 nm
Active area:	0.965 mm^2
Maximum responsivitity:	0.73 mV/nW
Supply voltage:	2.7 to 5 V
Saturation voltage:	4.95 V
Risetime:	30 μS
Noise voltage at 1kHz:	1 mV_{rms}

2.3.4 Custom made Gel box apparatus design

The conventional gel box where the electrophoresis takes place in is normally made of proxy glass, but in order to maximize the amount of UV light that interacts with fragments we needed high quality quartz glass to be placed in the detection zone. A custom made gel box that can transmit UV light and also locate the sensor and the detector was custom made. This apparatus is compatible with traditional electrophoresis appartus, light weight, compact, inexpensive, and adjustable placing for placing the UV source and an opening for placing the detector. With these

goals in mind, an existing gel box design was modified to incorporate a UV light source and a UV detector in a setup scheme as illustrated by Figure 9.

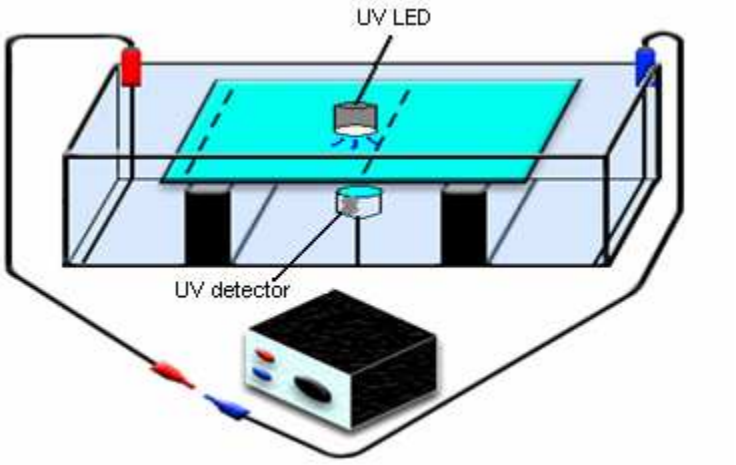

Figure 9: setup scheme of an UV detection enabled electrophoresis gel box.

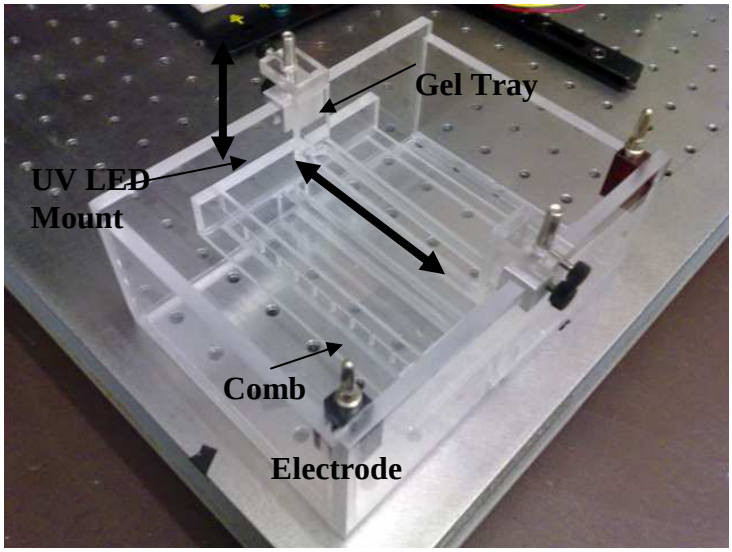

Figure 10: The first prototype of costume made gel box.

In the custom made gel box (Figure 10), the sensor is placed underneath the channels in the opening underneath the tray platform, and the UV source light is placed above the channels in a height adjustable mount. Also the gel tray and the center section of the tray platform are made of UV grade quartz, allowing UV radiation to reach the detector.

2.3.5 Testing method

A simple electrophoresis test was done with a 1Kbp DNA ladder. After preparing the 1 % Agarose gel solution with 3.5 mm thickness, a 1 mm channel width comb was inserted in to the gel for creating the separating channels. The test set up mimicked the electrophoresis apparatus at **Genome British Columbia**. The comb was removed after the gel solidified and the tray was placed in the electrophoresis unit with enough 10X Tris/Borate/EDTA (TBE) buffer to cover the gel. The detector was placed mid way of the gel box underneath the UV transparent quartz plate in the opening underneath the tray platform. The details on gel preparation used in the experiment are in Appendix 2. The gel was placed in the gel box (wells towards the negative electrode) and was filled with running buffer (700 ml of 1X TBE) until the gel is completely covered. Then to begin the electrophoresis experiment the gel box was connected to the power supply and run gel at 80-100 mV. The test was conducted as follows: two of the channels were loaded with DNA, one was in the path of the detection zone (where the detector and LED were placed) and the other one was tagged with a colored die to be able to visualize where the DNA fragments are roughly at, after the electrophoresis had begun.

One channel was loaded with 5ng of total DNA. In the channel directly between the LED and the detector, the first channel, only 5ngr of DNA ladder was loaded, whereas the second channel was loaded with Bromophenol blue dye. Bromophenol blue is usually used as a color marker to monitor the process of agarose gel electrophoresis. Since bromophenol blue carries a slight negative charge at moderate pH, it will migrate in the same direction as DNA or protein in a gel; the rate at which it migrates varies according to gel density and buffer composition, but in a typical 1% agarose gel in TBE buffer, bromophenol blue migrates at the same rate as a DNA fragment.

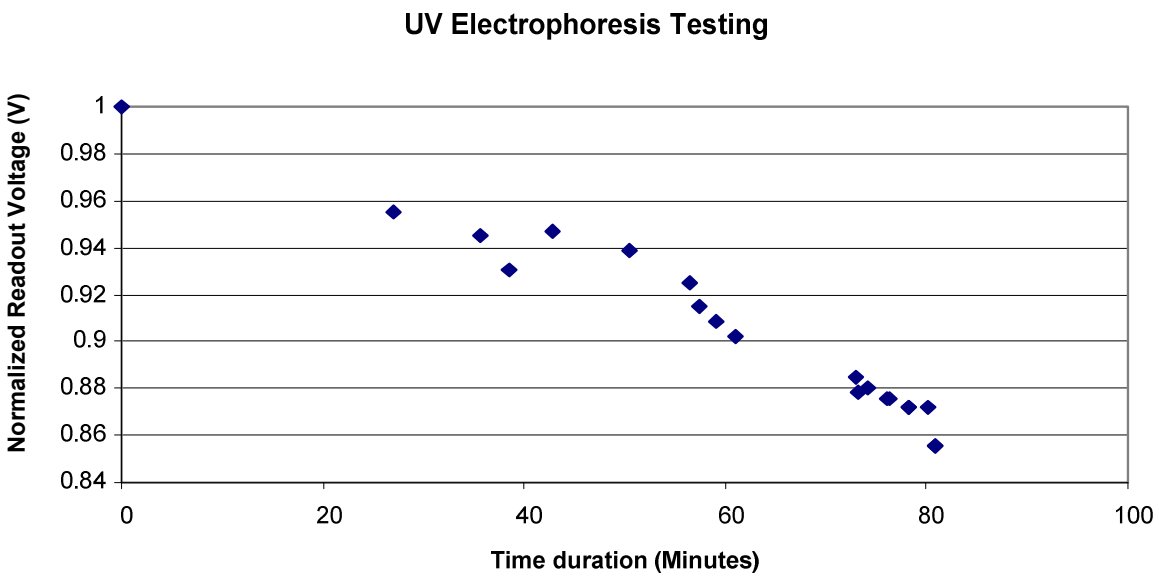

Figure 11 : Electrophoresis experiment with UV LED and detector, normalized voltage output readout versus readout time.

Figure 11, shows the graph of normalized voltage output versus time from the electrophoresis test with the proposed method. The first point shows the voltage output at the very beginning, i.e. sampling the gel without any DNA in the detection zone for calibration purposes as defined before. After this point, the channel with the colored die was monitored as an indication of where the DNA fragment is moving in the channel. From the readout of the sensor until about 20 minutes the readout was constant and the very first drop in sensor read out was observed at about 20 minutes past the start of electrophoresis testing. The next point shows the first voltage drop from the detector which was confirmed with the dye carrying channel. After this point whenever the voltage was changed a screen shot of the sensor readout was taken. As can be seen, after almost an hour the voltage drop is increasing which confirms that DNA's fragments with larger sizes are moving. The voltage drop can also infer higher concentration of DNA in the detection zone. To have a better understanding of this initial test and these results two more experiment

need to be done to monitor the changes of voltage drop for fragments with the same size but different concentration, and for fragments with the same concentration but different sizes.

This initial test was only conducted to prove the feasibility of the proposed methods; there were no computer or controllers to save the data and the readout was not fast enough because it was done by looking at the screen to observe a voltage drop and capturing the data when a voltage drop was seen. Therefore with this test alone the improvement in resolution can not be observed, therefore a future test set up with a controller and right detector size has to be conveyed to show the improvement in terms of resolution for electrophoresis fragment sizing. The detector and the readout are the main parts of the proposed method, and in the following section we will summarize the qualities that the detector must have to be used in the proposed method.

2.3.6 UV detector requirement for DNA fragment sizing application

According to [12], the biomedical sensors that are categorized as appliances for measuring or mapping a parameter within a given period are classified under medical imaging category. These sensors are generally computer controlled, and the cost of the sensor unit should be relatively low and not the determining factor. Minimum number of mask and easy steps of fabrication process for the sensor array will ensure low cost detectors. Another important factor is high throughput; therefore an array of detector with specific width and distances between them is required to maximize the number of loaded channels simultaneously. The distance between the sensors has to be the same as the distances between the separating channels and the width of the detector has to be the same size as the separating channel wells. Insertion of comb in the Agarose gel determines the channel wells as mentioned before, which can be of any size. Usually channels are 1mm wide and have 0.5 mm distance between them. Therefore as a requirement each detector has to be 1mm wide and the distances between the detector in the array has to be almost equal to 0.5 mm. In order to increase the resolution as much as possible the length of the detector becomes important. The smaller the detector's length the better resolution can be achieved. A length of 10μm is a good start, to test for improving the resolution.

Another important factor for ease of use in lab environment use is the selectivity of the sensor to 260nm and not to ambient light; enabling the gel electrophoresis analysis to be done in any environment without requiring specific conditions or filtering requirements. The sensors also have to be portable and have light weight for ease of use and placement in to the gel electrophoresis apparatus.

With these specifications in mind, next section will introduce a set of a-Si:H MSM photo detectors that are cost effective, easy to fabricate, flexible in size, selective to short wavelength (260 nm).

3 Chapter 3: a-Si:H MSM structures

3.1 Introduction

Each wavelength has a different absorption coefficient and penetration length for semiconductors, therefore modulating the thickness of the semiconductor layer allows higher sensitivity to specific wavelengths. In the short wavelength region of visible and UV spectrum, GaAsP Schottky diodes have received considerable attention. However, *pin* photodiodes using a-Si:H material have been reported to show a two-fold sensitivity improvement over GaAsP Schottky diodes in the UV region with a peak responsivity of 0.254 A/W at 385nm [13]. To date, different *pin* photodiode configurations with varying thickness of hydrogenated amorphous silicon carbide, a-SiC:H have also been reported [14] for UV detection. The wider bandgap of a-SiC:H shows higher selectivity to short wavelengths in the visible spectrum. However, the presence of carbon in the silicon network tends to increase the density of states. Thus, a lower quality film was obtained that offsets spectral selectivity the best responsivity result was 45 mA/W for wavelength lower than 300nm [14].

In comparison to *pin* photodiodes, a-Si:H photoconductor type detectors such as MSM are attractive because their fabrication process is simple and compatible with a-Si:H thin film transistors (TFT) where there is normally no *p* doped layer or a-SiC:H alloy incorporated [15]. In this chapter, we report on Metal-Semiconductor-Metal (MSM) photoconductor detectors (PD) fabricated using a-Si:H with a thickness optimized for short wavelengths of 260 nm. Experimental results of photocurrent measurements as well as responsivity and quantum efficiency for different a-Si film thickness, bias voltage and electrode gap are presented.

The majority of MSM-PD reported to date [16] possess top electrodes (TMSM-PD) and are illuminated from the top side which impedes part of the incident light hence reducing the device responsivity. In contrast, top illuminated bottom electrode MSM-PD (BMSM-PD) devices are attractive to avoid the reduction in responsivity. In the last part, we also report on a novel bottom illuminated a-Si:H TMSM-PD device fabricated on a quartz substrate with a high responsivity at 260 nm. The TMSM-PD device is also compatible with a tri-layer bottom gate staggered TFT fabrication process to enable imaging pixel arrays for biomolecular imaging applications.

3.2 Metal Semiconductor Metal (MSM) structures

Metal semiconductor metal photoconductors (MSM-PD), consists of Schottky or ohmic metal contacts in the form of integrated metal fingers on top or bottom of the semiconductor layer. Upon light illumination, photo generated carriers are swept out from the gap between the electrodes by the bias electric field and contribute to the photocurrent.

MSM photoconductors are biased such that one contact is forward biased (Anode) and the other one is reverse biased (Cathode). Upon light illumination, photons are absorbed by the semiconductor active layer by raising the potential energy of an electron in the valance band to the conduction band as is shown in Figure 12. Photo generated carriers are swept out from the gap between the electrodes by the bias electric field and would then contribute to the photocurrent.

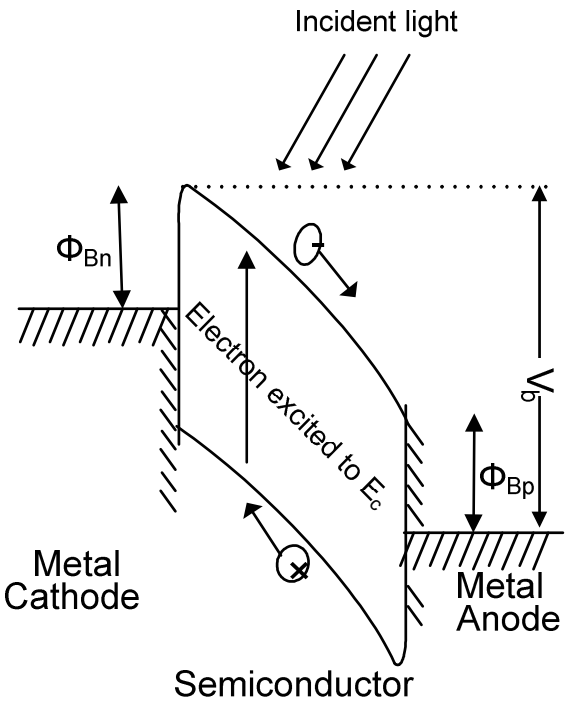

Figure 12: Potential energy diagram for an MSM-PD under bias.

The structure of a coplanar photoconductive photo detector is similar to a thin film transistor with no gate (Figure 12). Upon exposure to light, absorbed photons in the channel area create electron hole pairs and therefore channel conductance is modulated. The semiconductor film thickness determines photo detector selectivity; for very thin a-Si:H layer thickness, only a small portion of green and red light is absorbed, while most of blue and UV are absorbed and contribute to channel conductance modulation. Different device topologies have been proposed or reported as coplanar structure for photoconductor detectors [15], among which, the metal-a-Si:H-metal structure with ohmic or Schottky contacts were reported to have high sensitivity as well as compatibility in process with TFT fabrication (there is no p^+ layer involved, as is the case for photodiode detectors) [17]. Figure 13, shows schematic diagram of a coplanar photoconductor (center), as well as two different practical methods for its fabrication: bottom electrode and top electrode configuration. The top-electrode configuration is compatible with tri-

layer bottom gate staggered TFT fabrication (Figure 14) [18], while the bottom electrode structure is compatible with top-gate staggered TFT.

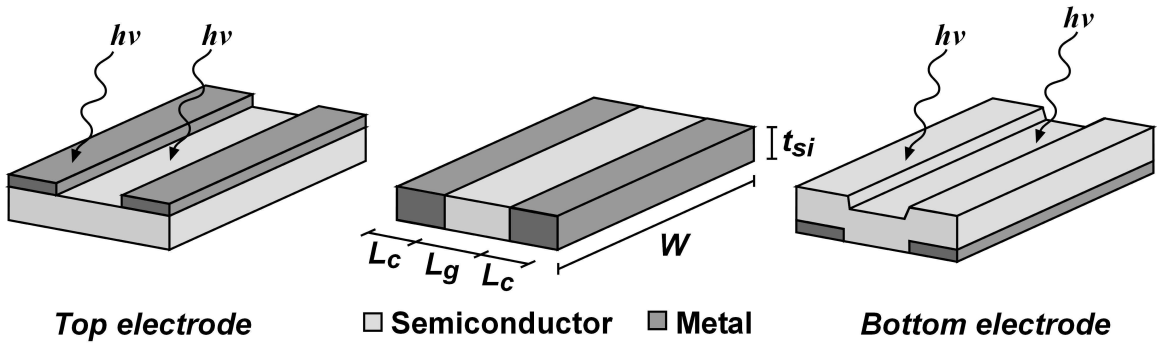

Figure 13 :Schematic diagram of coplanar photoconductor detectors; top electrode (left) and bottom electrode (right).

Figure 14: Bottom electrode configurations compatibility with top gate TFT fabrication.

3.3 MSM design consideration

For thin a-Si:H MSM structures to be most efficient at wavelength of consideration a more detailed look in to the design structure is necessary. One of the most important figures of merits is the η, intrinsic quantum efficiency (QE). Because of reflection from the surface, only part of incident photons enter the device, and if the photoconductor thickness is small, only part of the photons entering the device, are actually absorbed. Assuming all absorbed photons generate an electron-hole pair, η, is written as:

$$\eta = (1-R)(1-\exp(-\alpha t_{si})) \qquad \textbf{Equation 10}$$

In which $R=(n-1)^2/(n+1)^2$ is the surface reflectivity, α and n are wavelength dependent absorption coefficient and refractive index of the photoconductor material respectively [18], and t_{si} is the photoconductor material thickness. Intrinsic QE is material dependent quantity. Therefore in designing the MSM, choosing the right photoconductor material which has a low reflection from the surface in lower wavelengths and high absorption coefficients is a plus. Figure 15, shows the wavelength dependency of reflectivity and absorption coefficient of amorphous silicon which is the photoconductor material we chose in this research, and Figure 16, shows the calculated η for different values of amorphous silicon film thickness.

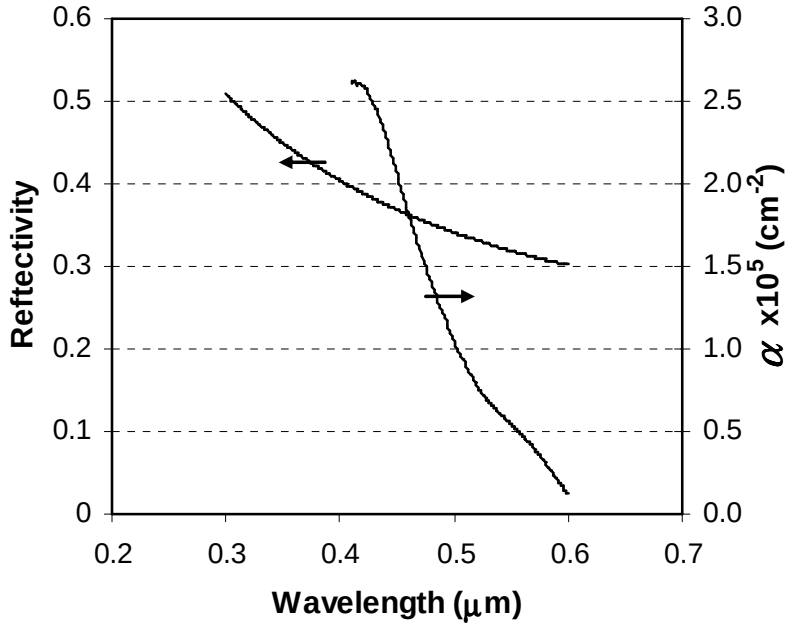

Figure 15: Wavelength dependency of reflectivity and absorption coefficient of amorphous silicon.

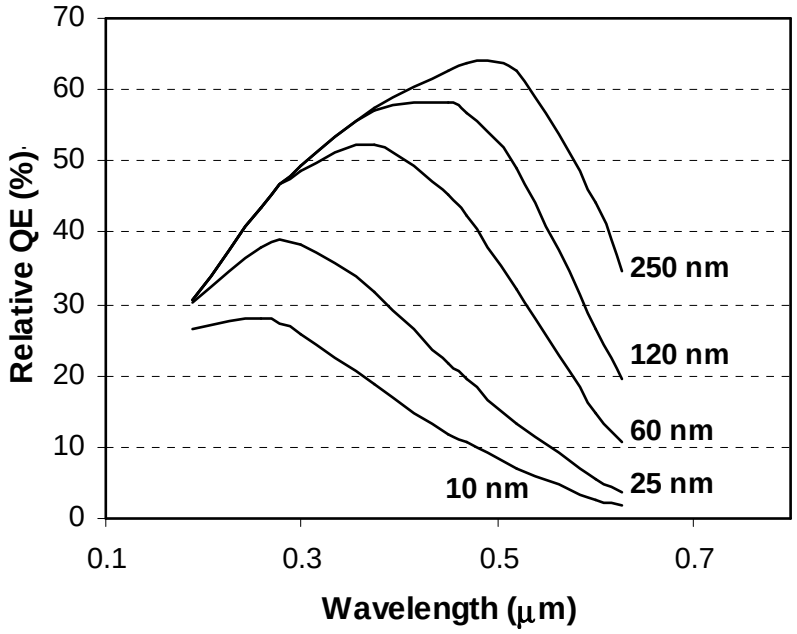

Figure 16: C**alculated intrinsic QE for different values of amorphous silicon film thickness.**

For lower thickness, higher η is achieved at lower wavelengths together with higher suppression at higher wavelengths. A film thickness of 25nm from this calculated result would give us highest η at 300nm wavelength. As was explained before η is a material dependent quantity, and in order to validate the performance of a dive another figure of merit should be introduce which is the external quantum efficiency (EQE). EQE is defined to be the ratio of charge flux to photon flux, shows how effectively the incident photon flux is converted to charge carriers, and how effectively those carriers are collected [19].

$$EQE = \frac{I_{ph} / q}{P_{inc} / h\nu}$$ **Equation 11**

3.4 MSM analysis

Assuming ohmic contacts and no space-charge-limited current, drift of optically generated carriers under externally applied electric field is the main mechanism of generating photocurrent in an illuminated coplanar photoconductor. In steady state condition, the density of excess carriers is equal to $G_{opt}\tau_r$, and if this value is much larger than intrinsic carrier concentration, the photocurrent is written in form of the standard drift equation as:

$$J_{ph} = qG_{opt}\tau_r\ \mu E \qquad \textbf{Equation 12}$$

in which q is the electronic charge, G_{opt}, optical generation, τ_r, effective recombination time, μ the carrier mobility, and E, the applied electric field. A photoconductor illuminated under optical power density of P_{opt}, receives a photon flux of $\Phi_{ph} = P_{opt} W L_g / h\nu$, in which W and L_g are photoconductor contacts width and the gap between them respectively, and $h\nu$, equal to hc/λ, is the photon energy. The optical generation is equal to absorbed flux of photons per volume. Therefore, assuming the intrinsic QE of amorphous silicon to be η, G_{op} in the active volume of the WL_gt_{si} between photoconductor contacts is found to be:

$$G_{opt} = \frac{\eta \Phi_{ph}}{WL_g t_{si}} = \frac{\eta P_{opt}}{h\nu\, t_{si}} \qquad \textbf{Equation 13}$$

Knowing that the area of the photoconductor through which photo current flows is Wt_{si}, and the applied electric filed is equal to V/L_g, Substituting (Equation 14) in (Equation 13) results in the photocurrent as:

$$I_{ph} = J_{ph} W t_{si} = q\,\eta \frac{\lambda P_{opt}}{hc} \mu\tau V \frac{W}{L_g}$$ **Equation 15**

Equation 14 is a1-D assumption which is valid if the photon absorption depth is much smaller than the distance between the adjacent metal fingers (L) [20]. In this 1-D approximation, a linear proportionality of the photocurrent to photoconductor aspect ratio, W/L_g, photoconductor biasing voltage, V, as well as, transport properties of the photoconductor, $\mu\tau$, and density of photon flux, $\lambda P_{opt}/hc$ is expected. However, because mobility-lifetime product is photon flux dependent, the photocurrent appears to be slightly sub-linear with respect to incident light intensity [21]. As a first order approximation, I_{ph} was taken to be linear with respect to the density of incoming photon flux, $\lambda P_{opt}/hc$ [15]. At high electric fields, where the device enters space charge limited current regime, photoconductor current becomes non-linear with respect to the applied voltage, however, linear approximation holds at low operating voltage points. The EQE with substituting the I_{ph}, and P_{inc} in the equation can be written as, where, A is taken to be the total illuminated area of the device:

$$EQE = \frac{I_{ph}/q}{P_{inc}/h\nu} = \frac{I_{ph}}{P_{opt} A} \frac{hc}{\lambda q} = \eta\mu\tau V \frac{W}{AL_g}$$ **Equation 16**

The theoretical expression of selectivity is obtained by substituting (Equation 10), and (Equation 14) and calculating the ratio of the detector photocurrent for two different wavelengths.

$$S = \frac{\lambda 1 (1 - R_{\lambda 1})(1 - \exp(-\alpha_{\lambda 1} t_{si}))}{\lambda 2 (1 - R_{\lambda 2})(1 - \exp(-\alpha_{\lambda 2} t_{si}))}$$ **Equation 17**

For optical power density of 184 μW/cm^2, and biasing voltage of 20 V, blue to green photocurrent selectivity, *S*, of fabricated detectors was measured to be 1.2 and 1.25 for detectors with 60 nm and 25 nm of a-Si photoconductor thickness respectively, which is comparable to calculated value of 1.18 and 1.35 respectively. However, for detectors with t_{Si} = 15 nm, measured values were neither consisting, nor following the expected trend. We concluded that bad quality of electrical contacts between very thin amorphous silicon film and side walls of patterned electrodes might be the reason for inconsistent characteristics of 15 nm thick samples.

3.5 MSM experimental results

A. Device Fabrication

Bottom electrode MSM (BMSM) coplanar photoconductors with three different amorphous silicon film thicknesses of 15, 25, and 60 nm were fabricated in house. First, 60 nm aluminum was sputtered on corning glass substrates, and was patterned using standard lithography and wet etching to have various electrode spacing (L_g) of 5, 10, 15, 20 and 30 μm, and contact length (L_c) of 10 μm. Hydrogenated amorphous silicon was next deposited using plasma enhanced chemical vapor deposition (PECVD), followed by a very thin silicon nitride layer to protect the photoconductor film from oxidation. Finally, silicon islands were patterned over electrodes using dry etching, (Table 4) and samples were annealed at 200°C in vacuum for an hour before any measurement.

Table 4: Step by step fabrication of BMSM.

Step	Description	Diagram
1	Aluminium sputtering on quartz substrate	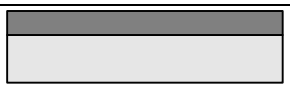
2	Patterning of the bottom electrodes using wet etching	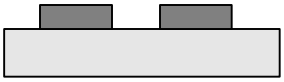
3	PECVD deposition of a-Si:H layer	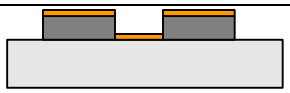
4	PECVD deposition of a-SiN_x	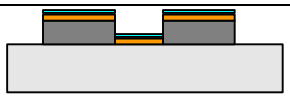
5	Patterning of active island using RIE	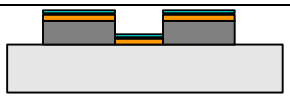
6	Opening pads vias	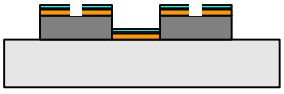

Table 5, summarizes the deposition conditions for both a-Si:H and a-SiN_x layers.

Table 5: Deposition Condition for PECVD films Used.

Film	Gas mixture	Flow rate (sccm)	Pressure (m Torr)	Temp. (°C)	Power (W)
a-Si:H	***SiH_4/H_2***	***20/100***	***500***	***250***	***1W***
SiN_X	***$SiH_4/NH_3/H_2$***	***2/16/100***	***1900***	***250***	***20W***

Figure 17 shows the bottom electrode MSM with various electrode spacing (L_g) of 5, 10, 15, 20 and 30 μm, and contact length (L_c) of 10 μm.

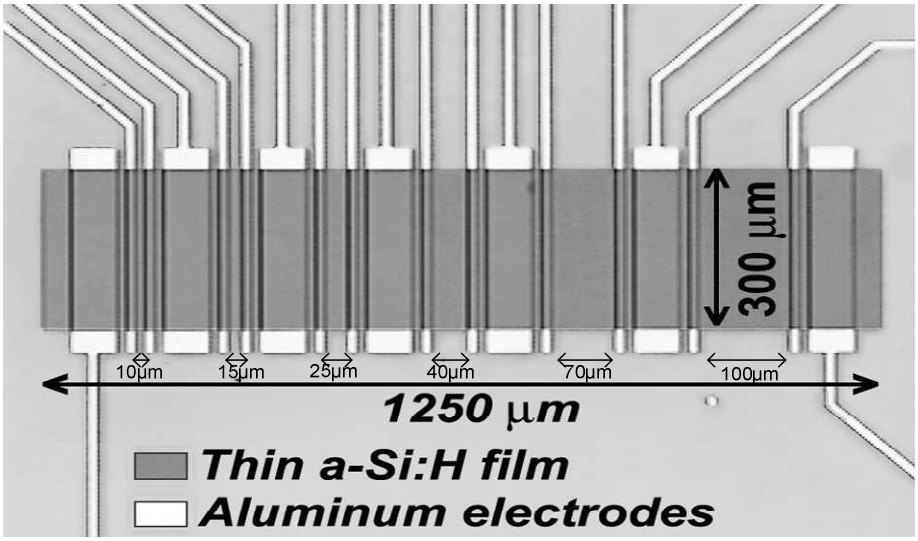

Figure 17: Photomicrograph of fabricated photoconductor photodetectiors with different electrodes spacing of 5, 10, 15, 20, 30, 50, 100 and 150 µm; all devices have the same width of 300 µm. Results on devices with electrode spacing of 5 to 30 µm are reported here.

Also, we fabricated a set of top electrode MSM (TMSM) with 25 nm thick a-Si:H active layer. For the TMSM-PD structure, a-Si:H film was deposited first, followed by 60nm of sputtered aluminum without breaking the vacuum. Wet etching was used to pattern the aluminum electrodes, followed by deposition of a protective silicon nitride film and a-Si:H island patterning. (Table 6)

Table 6: Step by step fabrication of TMSM.

Step	Description	Diagram
1	PECVD deposition of a-Si:H layer	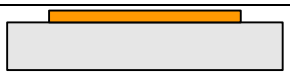
2	60 nm Aluminium sputtering	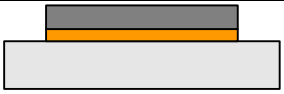
3	Patterning of the top electrodes using wet etching	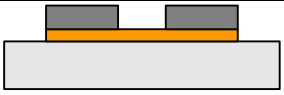

4	PECVD deposition of a-SiN_x	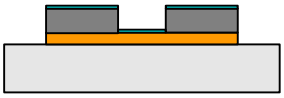
5	Patterning of active island using RIE	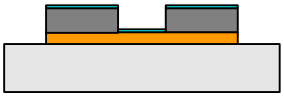
6	Opening pads vias	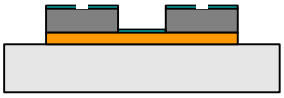

B. Device results and discussion

Blue light responsivity of photoconductors with different gap between electrodes of BMSM was measured versus bias voltage (Figure 18).As expected, close to linear dependency of responsivity to bias voltage was observed. For shortest gap between electrodes, i.e., L_g = 5µm, responsivity as high as 180 mA/W for blue light was measured which is comparable to or better than reported values for other detectors [22].

Figure 18, also confirms a linear relationship for low voltages between photocurrent and voltage which confirms our assumption of ohmic contacts. Therefore the linear dependency of I_{ph} with V is valid and from Equation 15 the mobility lifetime of the device can be extracted.

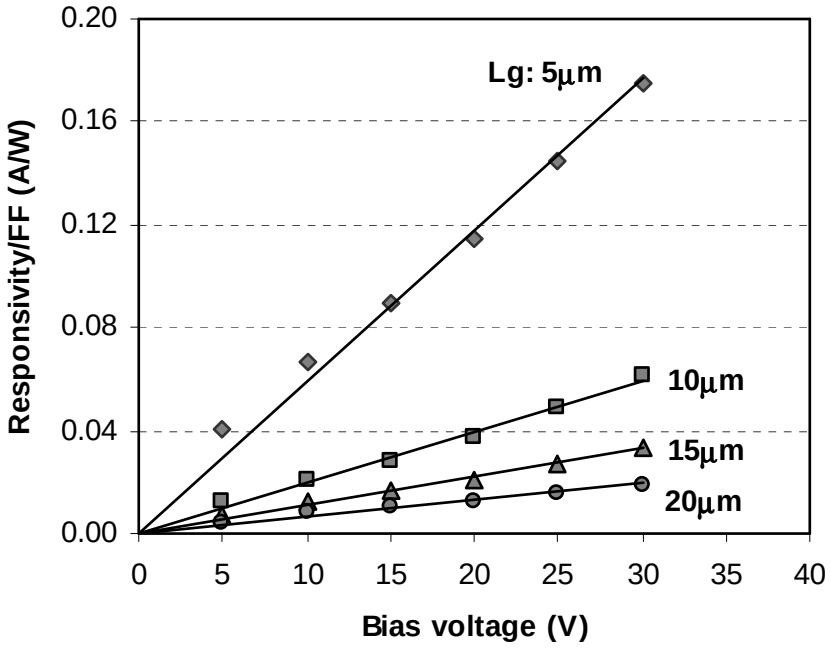

Figure 18 : Measured blue responsivity of the 25 nm thick photoconductor versus biasing voltage for different electrode spacing. The blue responsivity is as high as almost 180 mA/W for electrode spacing of 5 micrometer.

The responsivity of the detector for three different colors of RGB (Red, Green, and Blue) was measured as shown in Figure 19. Photoconductors do not show a linear response over a wide range of input optical signal but at low input photon flux, the response is fairly linear. Bearing in the mind that the input for the reported devices is limited in range and the flux is low, a first degree approximation (linearity of response) was used to derive the photocurrent. The same approach is used in [23].

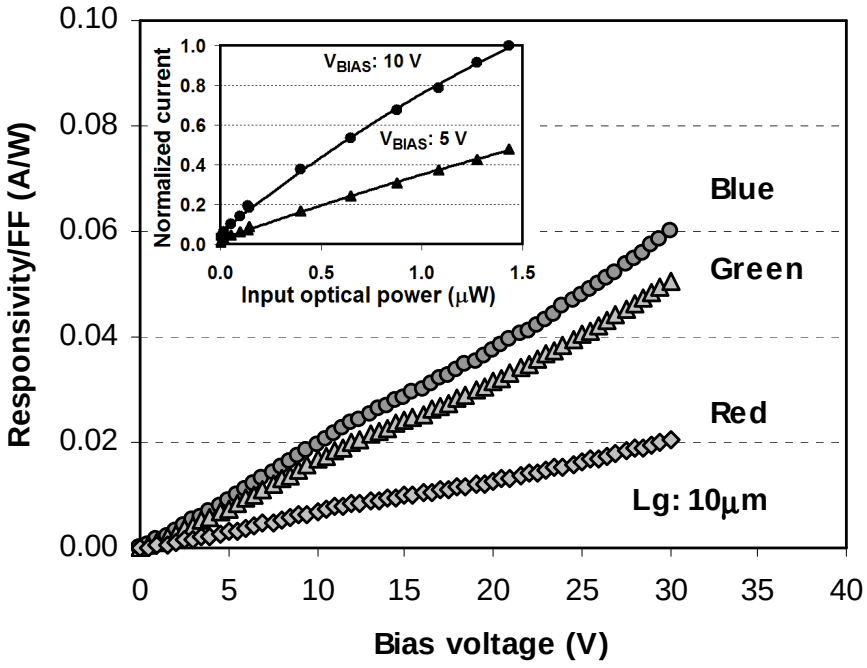

Figure 19: RGB responsivity with L_g of 10μm, and also photocurrent versus optical power of blue light.

The extrinsic mobility lifetime product was extracted from calculation of slope of photo current versus applied bias voltage, $\Delta I_{ph} / \Delta V$, and versus inverse of gap between electrodes, $\Delta I_{ph} / \Delta(1/L_g)$. The result is shown in Figure 20, where mobility lifetime product reaches its maximum value for 10μm gap between electrodes. For photovoltaic type photodetectors such as *pin* diodes, carriers move perpendicular to the substrate, hence, they do not experience the substrate surface roughness, and are not trapped in surface states compared to carriers moving in coplanar detectors. For very thin films, the surface states on the top and bottom interfaces of the narrow conduction channel play a major role in trapping of carriers, which results in low mobility-lifetime product. The lateral flow of charge carriers, parallel to the substrate, also forces the carriers to follow the roughness of the substrate which is another cause of increased trapping and subsequently, a low mobility-lifetime product. Therefore it is expected that the mobility lifetime product to be low, especially for very thin a-Si layers. It is observed that the mobility life

time product slightly increases as the gap between electrodes decreases. This is probably due to reduced chance of trapping in surface states. Assuming recombination time of 10^{-7} s, the mobility would be 0.3 cm^2/Vs for 10μm electrode gap devices which is in the expected range for a-Si.

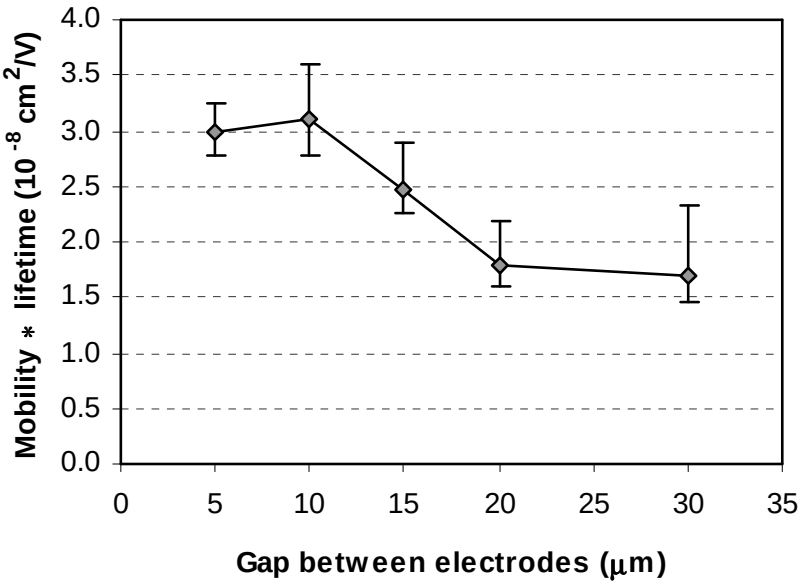

Figure 20: Extracted mobility lifetime product from photocurrent measurements for different gap between electrodes. The $\mu\tau$ product is maximum value for L_g = 10μm.

As expressed in Equation 16, EQE is a function of gap between electrodes and applied voltage, as well as contact length, L_c. For maximum EQE at short wavelength from Equation 10, a thickness of 25nm was chosen. To suppress the effect of contact length, the ratio of quantum efficiency to fill factor (FF), i.e., EQE/FF is plotted in Figure 21. Quantum efficiency greatly improves as the gap between electrodes becomes smaller. However, the ratio of illuminated current to dark current, $R_{L/D}$, decreases for smaller values of L_g. This is due to the fact that for a photoconductor under illumination, fewer holes are trapped because of photon bombardment and therefore, the photo current is not space-charge-limited as the dark current is. Assuming photocurrent to be proportional to $1/L_g$ (Equation 15), and dark current to be proportional to $1/L_g^2$

[24], then $R_{L/D}$ would be proportional to L_g. The spectral quantum efficiency shows considerably higher values for blue than green, as the spectral responsivity was.

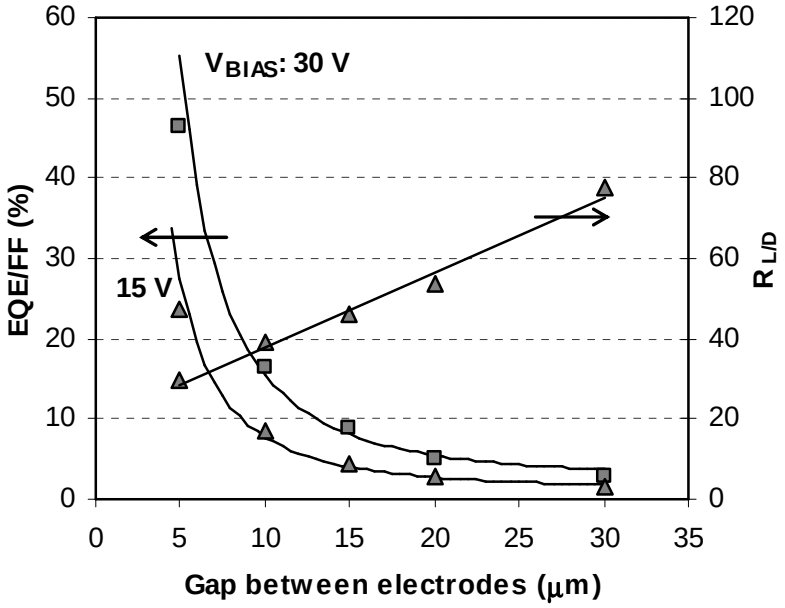

Figure 21: Calculated (solid) and measured values (dots) of EQE of fabricated photoconductors for two biasing voltage of 15 and 30V versus gap between electrodes.

Figure 22, shows the EQE for different wavelengths, from Equation 10 and Equation 16, it is expected that EQE peaks at about 300nm of wavelength.

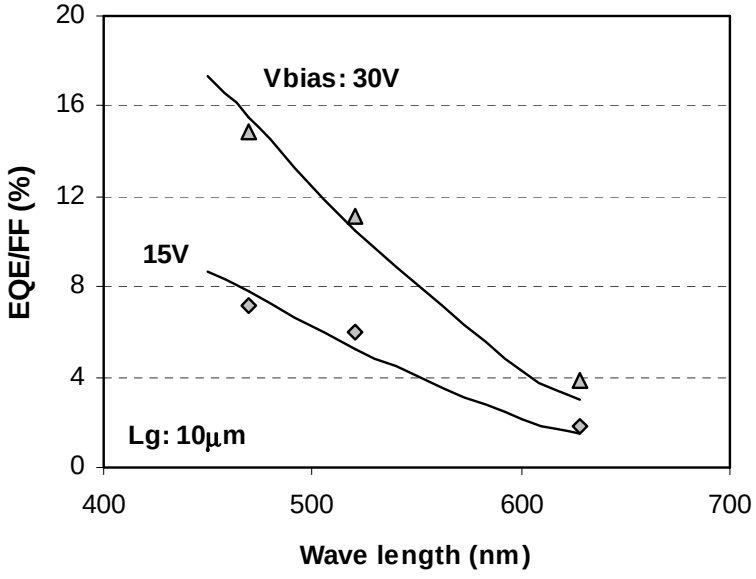

Figure 22: Calculated (solid) and measured values (dots) of EQE of fabricated photoconductors for two biasing voltage of 15 and 30V versus different wavelengths.

So far all the presented results were from a-Si:H BMSM that were illuminated from top. The majority of MSM-PD reported to date [16] possess top electrodes (TMSM-PD) and are illuminated from the top side which impedes part of the incident light hence reducing the device responsivity. In contrast, top illuminated bottom electrode MSM-PD (BMSM-PD) devices are attractive to avoid the reduction in responsivity.

At this part, we report a novel bottom illuminated a-Si:H TMSM-PD device fabricated on a quartz substrate with a high responsivity at 260 nm. Comparing the results of TMSM and BMSM , the former shows better responsivity and EQE for 260 nm UV light. From the above results we decided to use 10 µm electrode spacing (L_g) between channels, and both TMSM-PD and BMSM-PD photoconductors were biased between 0 to 30V. Figure 23, compares the photo response and dark current of TMSM-PD and BMSM-PD as a function of dc bias voltage. In both structures the majority of absorption in the very short wavelength region is on the surface very close to the metal semiconductor interface. Usually MSM exhibits low external quantum efficiency (EQE) due to the shadowing of the contact which can limit the incident light from reaching the active region [25]. Thus back illuminating the TMSM-PD and top illuminating the BMSM-PD allows one to maximize the absorption to a region which is depleted by the planar electrodes. Also by doing so, the same area of each detector is illuminated. Although the dark current of both TMSM-PD and BMSM-PD are almost equal and very high, the photocurrent of TMSM-PD is higher for 260nm wavelength than BMSM-PD.

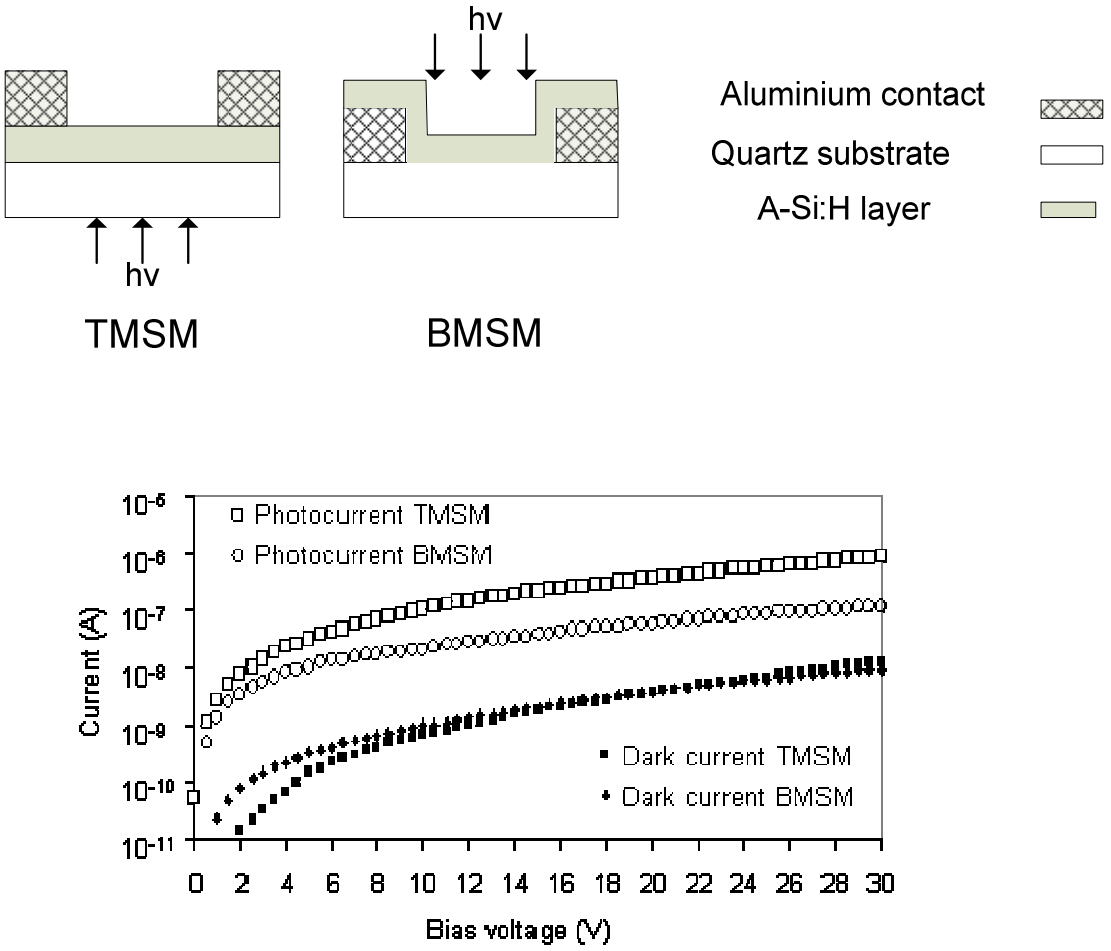

Figure 23. Schematic diagram, dark and photocurrent with illumination of 260nm UV light of power 0.05mW of TMSM-PD and BMSM-PD detectors.

Figure 24, compares the responsivity of TMSM-PD and BMSM-PD; for the three wavelengths of UV 260nm, blue 469nm, and red 628nm, the resposivity of TMSM-PD are approximately 10 times higher than that of BMSM-PD which was reported previously [25,26]. The highest responsivity was measured for TMSM-PD for 260nm light to be 150 mA/W under 20V biasing. Another figure of merit is the External Quantum Efficiency (EQE), which shows how effectively the incident photon flux is converted to charge carriers, and how effectively those carriers are collected; thus convolving effects of surface reflections and absorption constant of the photoconductor.

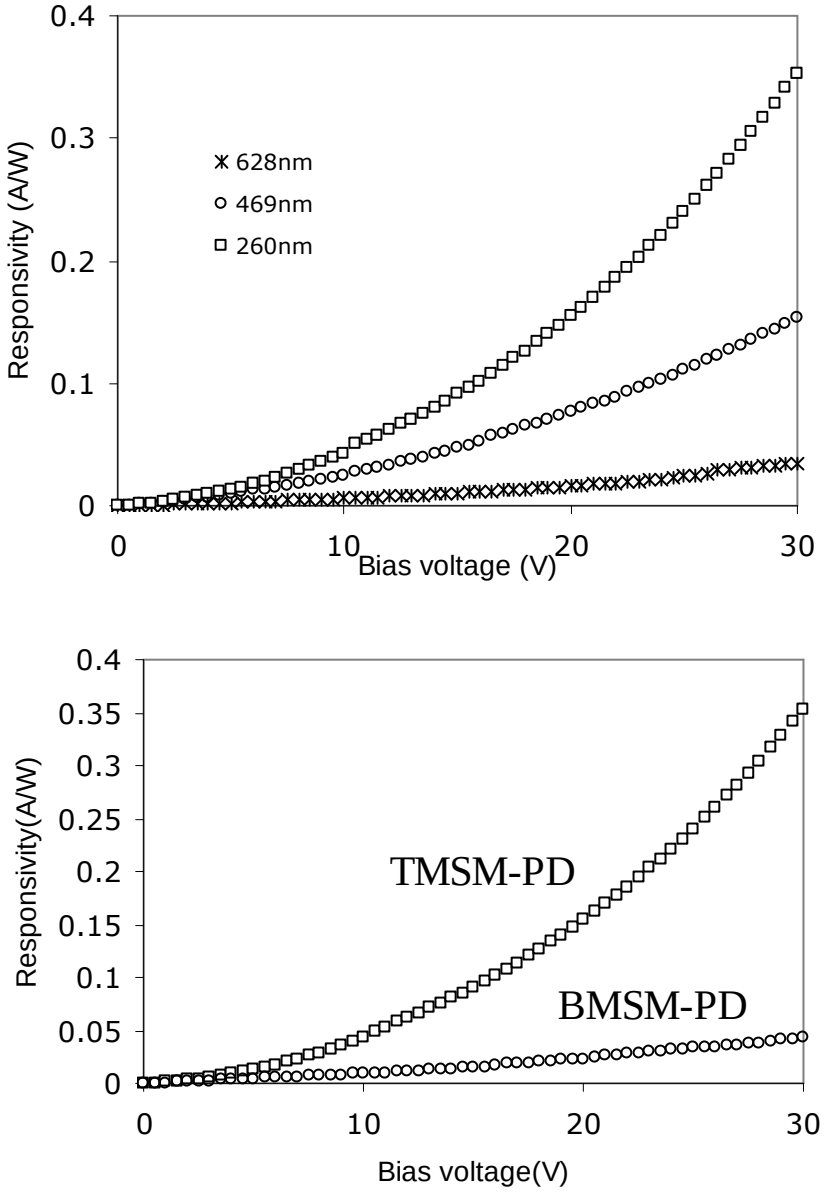

Figure 24. Responsivity of TMSM-PD with back illumination for three different wavelengths; and comparison of responsivity of TMSM-PD (back illumination) and BMSM-PD (top illumination) to only 260nm UV light.

Figure 25, shows the EQE of TMSM-PD for different voltages and they are evidently better than the previously reported results of BMSM-PD [26]. One reason for the better performance of TMSM-PD is the photo generated carriers on top of electrodes in BMSM-PD photoconductors

are not effectively collected due to the lack of a uniform channel with respect to the applied electric field, especially for very thin semiconductor layers in the order of 10 to 20 nm. The main mechanism of photo generated current is drift of optically generated current with the external applied field; therefore a more coplanar structure such as TMSM-PD in this case enables a better channel for these carriers to drift in.

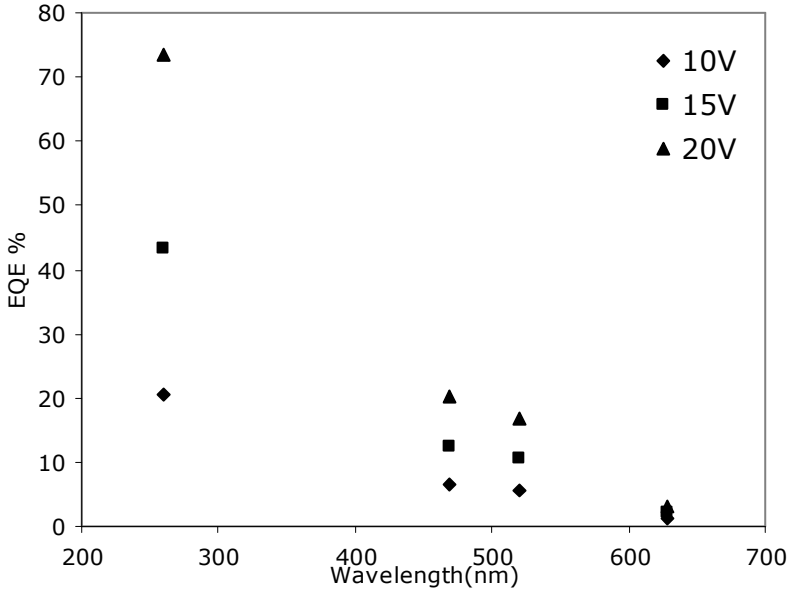

Figure 25. EQE of TMSM-PD with back illumination for three different wavelengths with varying the voltage.

Also, the aluminum contacts in TMSM-PD are deposited on top of the amorphous layer with out breaking the vacuum, which makes the semiconductor-metal interface better. The most obvious difference between the two is their geometry, for which the 25nm a-Si:H layer is more even and paved in TMSM-PD than BMSM-PD, also the superior contact formation between a-Si:H film and aluminum contacts makes the electric field which is responsible for carrying the charges over the channel more uniform and will lead to less recombination of carriers and make a difference in photocurrent responses.

4 Chapter 4: Conclusion

A new fast method for performing gel electrophoresis for bio-molecular fragment sizing using UV radiation is introduced in this thesis. Initial tests to validate the feasibility of the proposed methods were performed. Based on these tests, requirements for the UV detector were obtained. An MSM photo detector made of very thin a-Si:H film was used as a photo-detector, because of its simple fabrication and excellent performance especially at UV spectrum. We have reported the electrical characteristics, optical selectivity and quantum efficiency of MSM photo-detectors using very thin a-Si:H layers with aluminum electrodes having different gaps between them. Also, we have measured the performance of in-house fabricated photo-detectors at different biasing voltages, and under different monochromatic illumination for different electrode spacing. Expected values and measured data exhibit a close match. For detectors with 25 nm thick a-Si layer and 5 μm gap between electrodes, biased at 30V, a higher sensitivity in the blue region (as compared to the green and red) of the spectrum was measured, a responsivity reaching 0.176 A/W, and an EQE of more than 45%. We also studied the electrical characteristics, optical selectivity and quantum efficiency of TMSM-PD and compared it to BMSM-PD photodetectors for very thin a-Si:H layers, and aluminum electrodes. For TMSM-PD with 25 nm thick a-Si layer and 10 μm gap between and bottom illumination responsivity of 150 mA/W, and EQE of about 74% was measured for 260nm wavelength biased at 20V. The fabrication of the presented a-Si:H MSM photodetectors is fully compatible with state-of-the-art a-Si TFT fabrication processes, which can result in potentially low cost fabrication of highly selective short wavelength for bio-molecular fragment sizing using a TFT based imaging array.

5 Chapter 5: Publication and Patents from this work

1 M. Malhotra, F. Taghibakhsh, **I. Khodami**, M. Adachi, L. Tse, K.S. Karim, “Analysis of Leakage Current in a-Si:H p-i-n Diodes Prepared by Hot Wire Chemical Vapor Deposition,” The Twelfth Canadian Semiconductor Technology Conference, August 2005.

2 **I. Khodami**, M. Adachi, M. Malhotra, F. Taghibakhsh, K.S. Karim, K. Kavanagh, John A. Rowlands, “Light induced degradation in amorphous silicon photodiodes and implications for diagnostic medical imaging applications”, SPIE, International Medical Imaging Symposium, February 2006.

3 **I. Khodami**, M.M. Adachi, K.L. Kavanagh, K.S. Karim, "Wavelength selective amorphous silicon photodiodes for biomedical applications," 29th Canadian Medical and Biological Engineering Conference, June 2006.

4 W. F. L. Tse, **I. Khodami**, M. M. Adachi, X. Wang, K. Kavanagh, K.S.Karim, “Characterization of Low Temperature P-type Hydrogenated Nanocrystalline Silicon Thin Films,” in 2007 Canadian Conference on Electrical and Computer Engineering (CCECE), Dec 2006.

5 W. F. L. Tse, **I. Khodami**, K. Kavanagh, K.S.Karim, “Characterization of low temperature p^+ nc-Si:H window layers” To be submitted, January 2007.

6 F. Taghbibakhsh ,**I. Khodami**, K.S.Karim, “Characterization of Short Wavelength Selective a-SiH MSM Photoconductors for Large Area Digital Imaging Applications”,IEEE Transaction on electron devices, accepted July 2007.

7 **I. Khodami,** F. Taghibakhsh, K.S. Karim, “Ultraviolet Selective a-Si:H MSM Photodetector for Biomedical Applications” IEE electron device letters, to be Submitted December 2007.

Patents

1 Fragment sizing using short wavelength radiation for bio-molecular applications- filled October 29, 2007.

2 Short wavelength selective MSM detector with a-Si:H technology – In process.

Reference:

[1] E Monroy, F Omnes, F Calls “Wide-bandgap semiconductor ultraviolet photodetector” Seminconductor Science And Technology, vol. 18, pp. R33-R51, 2003

[2] C. Guiducci, C. Stagni, M. Brocchi, M. Lanzoni, B. Riccò, A. ascetti, D. Caputo, G. de Cesare “Innovative Optoelectronic Approaches to Biomolecular Analysis with Arrays of Silicon Devices”, IEEE, International Conference on Very Large Scale Integration of System-on-Chip. pp. 169 – 174, October 2006.

[3] A. D. Wilson and Lyall, “Design of an ultraviolet radiometer. 1: Detector electrical characteristics,” Appl. Opt. 25, 4530, 1986.

[3] D.Caputo, G. Cesare, F.Irrera, F. Palma, “Solar-blind UV photodetectors for large area applications” IEEE transactions on electron devices, vol. 43, No. 4, pp. 1351-1356. Sept 1996.

[4] A.Madan, “Amorphous silicon- from doping to multi billion dollar applications” Journal of non-crystalline solids 352, pp. 881-886, 2006.

[5] Powell M.J , French I.D. , Hughes J.R., Bird N.C., Davies O.S., Glass C. , Curran J.E. “Amorphous silicon image sensor arrays” Amorphous Silicon Technology Symposium, pp. 1127-37, 1992.

[6] Amirkhanian, V.D., Ming-Sun Liu “Multi-capillary electrophoresis disposable cartridge for bioseparations” Proceedings of the SPIE - The International Society for Optical Engineering, v 4966, pp. 92-7, 2003.

[8] Maniatis, T., Fritsch, E. F., Sambrook, J., Molecular Cloning: ALaboratory Manual, Cold Spring Harbor Laboratory Press,Cold Spring Harbor, NY 1983.

[7] Amirkhanian V.D, Ming-Sun Liu, U.S. patent application Ser. No. 10/059,993 entitled "Optical detection in a multi-channel bio-separation system" Document Type and Number: United States Patent 6828567.

[8] http://www.roithner-laser.com/All_Datasheets/LEDs/UVTOP265.pdf

[9] http://www.eoc-inc.com/ifw/JIC%20167-9%20B%200303.pdf

[10] Harsanyi, G. "Sensors in biomedical applications. May they change the quality of life?" Sensor review, v 21, n 4, pp. 259-67, 2001.

[11] Y.K.Fang, Sheng-Beng Hwang, Kuin-Hui Chen, Ching-Ru Liu, Ming-Jang Tsai, and Lee-Ching Kuo, "An amorphous SiC/Si Heterojunction p-i-n diode for low-noise and high-sensitivity UV detector", IEEE transaction on electro devices, vol. 38, No.2, pp. 292, 1992.

[14] de Cesare, G. ; Caputo, D.; Nascetti, A.; Guiducci, C.; Ricco, B. "Hydrogenated amorphous silicon ultraviolet sensor for deoxyribonucleic acid analysis" Applied Physics Letters, v 88, n 8, 20, pp. 83904-1, Feb. 2006.

[15] A.M. Castillo, A.T. Jacome, A. Heredia, R. Ramos, "An a-SiGe:H,F based thin film MSM high-speed photodetector", Proceedings of the 6th International Caribbean Conference on Devices, Circuits and Systems, pp. 91-94, 2006.

[16] Sang-Woo Seo, Sang-Yeon Cho, Sa Huang, Jeng Jung Shin, Nan Marie Jokerst, April S. Brown, Martin A.Brook, "High-Speed Large Area Inverted InGaAs Thin film Metal-Semiconductor-Metal Photodetectors", IEEE Journal of selected topics in quantum electronics, vol. 10, NO. 4, pp. 686 – 693, 2004.

[17] Laih, L.-H.; Chen, Y.-A.; Tsay, W.-C.; Hong, J.-W., "High responsivity a-Si:H bottom-electrode metal-semiconductor-metal photodetector", Electronics Letters, vol. 32, issue 10, pp. 929 – 930, 1996.

[18] D.B. Thomasson, T.N. Jackson, “Fully self-aligned tri-layer a-Si:H TFT with ultra-thin active layer”, IEEE Electron Device Letters,, vol. 18, no. 8, August 1997.

[19] M.C. Hamilton, J. Kanicki, “Organic polymer thin-film transistor photosensors’, IEEE Journal of Selected Topics in Quantum Electronics, Vol. 10, No. 4, pp. 840-848, July/August 2004.

[20] Shu Wu and Sung-Mo Kang, “Modeling and Simulation of Metal-Semiconductor-Metal Photodetector using VHDL-AMS”, Proceedings IEEE International Behavioral Modeling and Simulation Conference, pp. 59-63 IEEE 2004.

[21] R.E. Stearns, R.L. Weisfield, “Two dimensional amorphous-silicon photoconductor array for optical imaging,’ Journal of Applied Optics, vol. 31, no. 32, pp. 6874-6881, November 1992.

[22] M. Krause, M. Topič, , H. Stiebig, H. Wagner, “Thin-Film UV Detectors Based on Hydrogenated Amorphous Silicon and Its Alloys”, Physica Status Solidi (A), Applied Research, vol. 185, issue 1, pp.121-127, 2001.

[23] M. Shur, Physics of Semiconductor Devices, chap. 5, Photonic Devices, pp. 502, 1st edition, Prentice Hall, 1990.

[24] J. Sworakowski, G.F. Ferreira, “Space-charge-limited current and trap-filled-limit in one dimensional insulators,”*Applied Physics Letters*, vol. 17, pp. 135-139,1984.

[25] Sang-Woo Seo, Sang-Yeon Cho, Sa Huang, Jeng Jung Shin, Nan Marie Jokerst, April S. Brown, Martin A.Brook, “High-Speed Large Area Inverted InGaAs Thin film Metal -Semiconductor-Metal Photodetectors”, IEEE Journal of selected topics in quantum electronics, vol. 10, NO. 4, pp. 686 – 693, 2004.

[26] F. Taghbibakhsh ,I. Khodami, K.S.Karim, “Characterization of Short Wavelength Selective a-SiH MSM Photoconductors for Large Area Digital Imaging Applications”,IEEE Transaction on electron devices, accepted July 2007.

[27] F.H Karg et al., " Investigation of variously composed p/I junction in amorphous silicon solar cells by time of flight and spectral response measurements" Conference record of the 20th IEEE pp. 149, 1998.

[28] Hong Zhu and Stephan j. Fonash, "Study of buffer layer desing in single junction solar cells" *25th PVSC IEEE*, pp. 1097, 1996.

[29] Williams,David B.(David Bernard), 1949-, "Transmission electron microscopy : a textbook for materials science.c1996.

[30] U. Das, S. Morrison, E. Centurioni and A. Madan, "Thin film silicon materials and solar cells grown by pulsed PECVD technique," IEE Proceedings-Circuits, Devices and Systems, vol. 150, pp. 282-6, 08/05. 2003.

[31] Chang Hyun Lee and Koeng Su Lim, "A novel p-type nanocrystalline is buffer at the p/i interface of a-Si solar cells for high stabilized efficiency," in Amorphous and Heterogeneous Silicon Thin Films: Fundamentals to Devices - 1999. Symposium, pp. 507-12 April 1990.

[32] J. K. Rath and R. E. I. Schropp, "Incorporation of p-type microcrystalline silicon films in amorphous silicon based solar cells in a superstrate structure," Solar Energy Mater. Solar Cells, vol. 53, pp. 189-203, May 1998.

[33] A. Gordijn, J. K. Rath and R. E. I. Schropp, "High temperature n- and p-type doped microcrystalline silicon layers grown by VHF PECVD layer-by-layer deposition," in Amorphous and Nanocrystalline Silicon-Based Films - 2003 Symposium, 22-25 April 2003, pp. 637-42.

Appendix A

A.1 Electrophoresis gel preparation

To a 1% (weight/volume) (25 ml solution), weighed out approx. 0.25g of Agarose powder (biochemical grade), 2.5 ml of 10 X TBE solutions was added. Then the mixture was heated in microwave for approx. 30 seconds at high power (the agarose powder needs at least 80 degrees celcius to dissolve). The solution was lightly swirled to ensure proper mixing. Then the well-forming combs were placed and we waited at room temperature until gel cools comb down and solidified (approx. 15 -20 minutes); then the comb was carefully removed.

Detail information on the 1 Kb DNA ladder:

Concentration: 10µg/µl

Size: 250µg

Store at -20ºC

Detail information on the Agarose Powder:

Company Name: BioShop

Biochemical Grade

Gel Strength: >1200g/cm^2

Gelling Range: 36-39 degrees Celsius

Melting Range: 87-89 degrees Celsius

Detail information on the Buffer: 10X TBE

0.9 Moles/Liter Tris(Hydroxymethyl) Amino methane

0.9 Moles/Liter Boric Acid

0.02 Moles/Liter Ethylenedinitrilotetraacetic acid

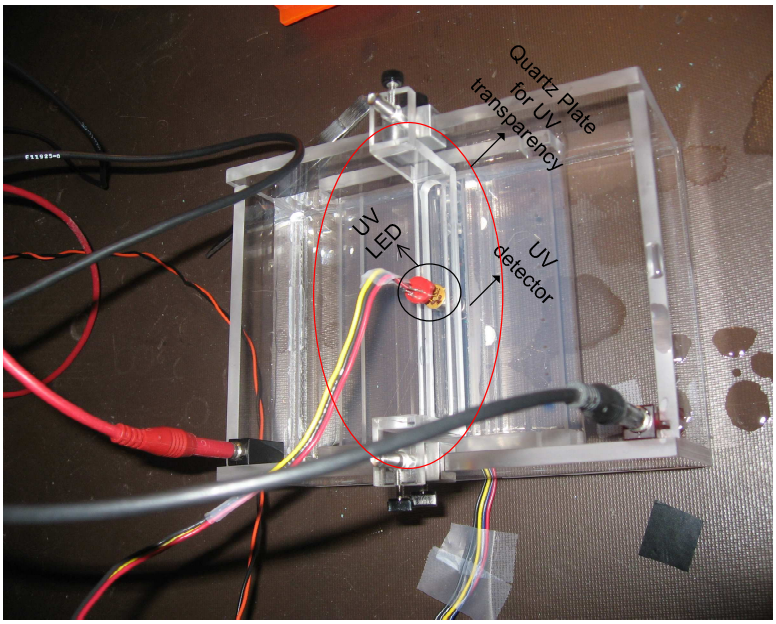

Figure 26: The first prototype of costume made gel box.

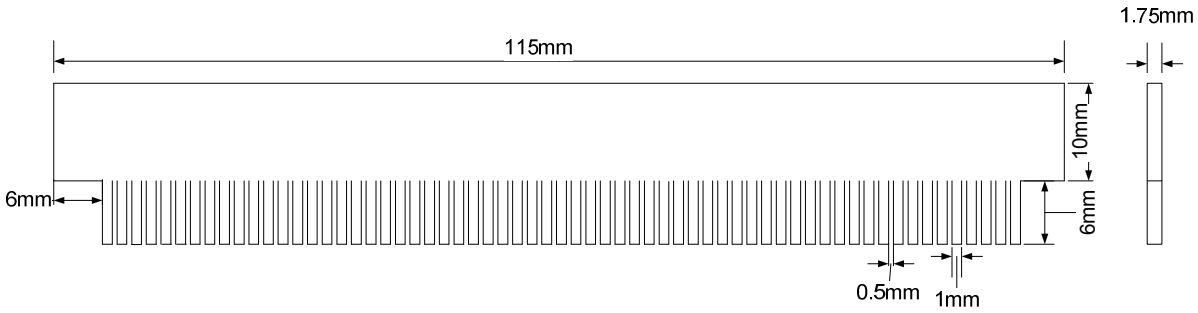

Figure 27: Side drawing of the comb with defined 1mm wells and o.5 mm spacing between the wells.

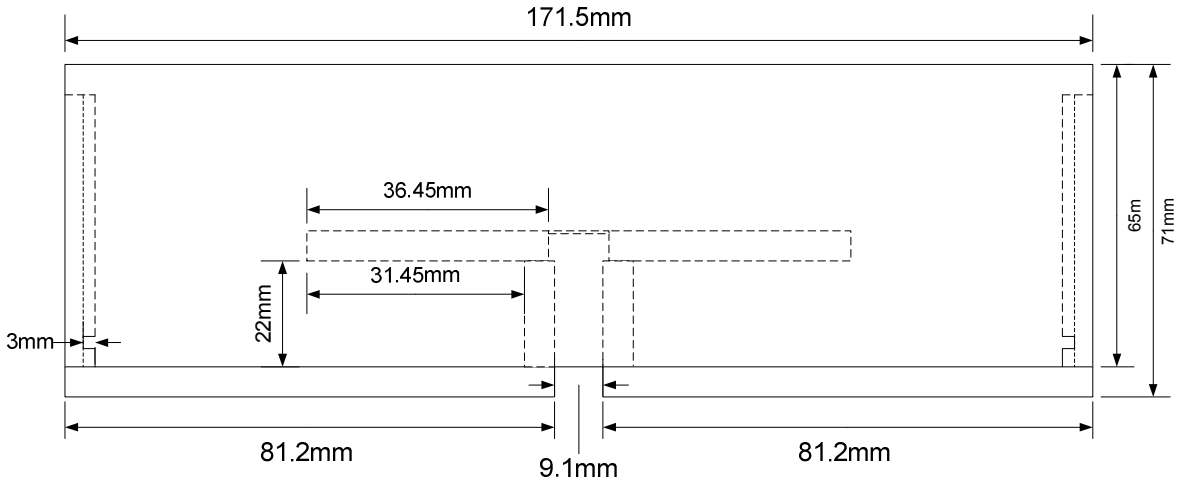

Figure 28: Side view drawings of the costume made gel box, with opening window for placing the sensors underneath with 9.1mm opening window.

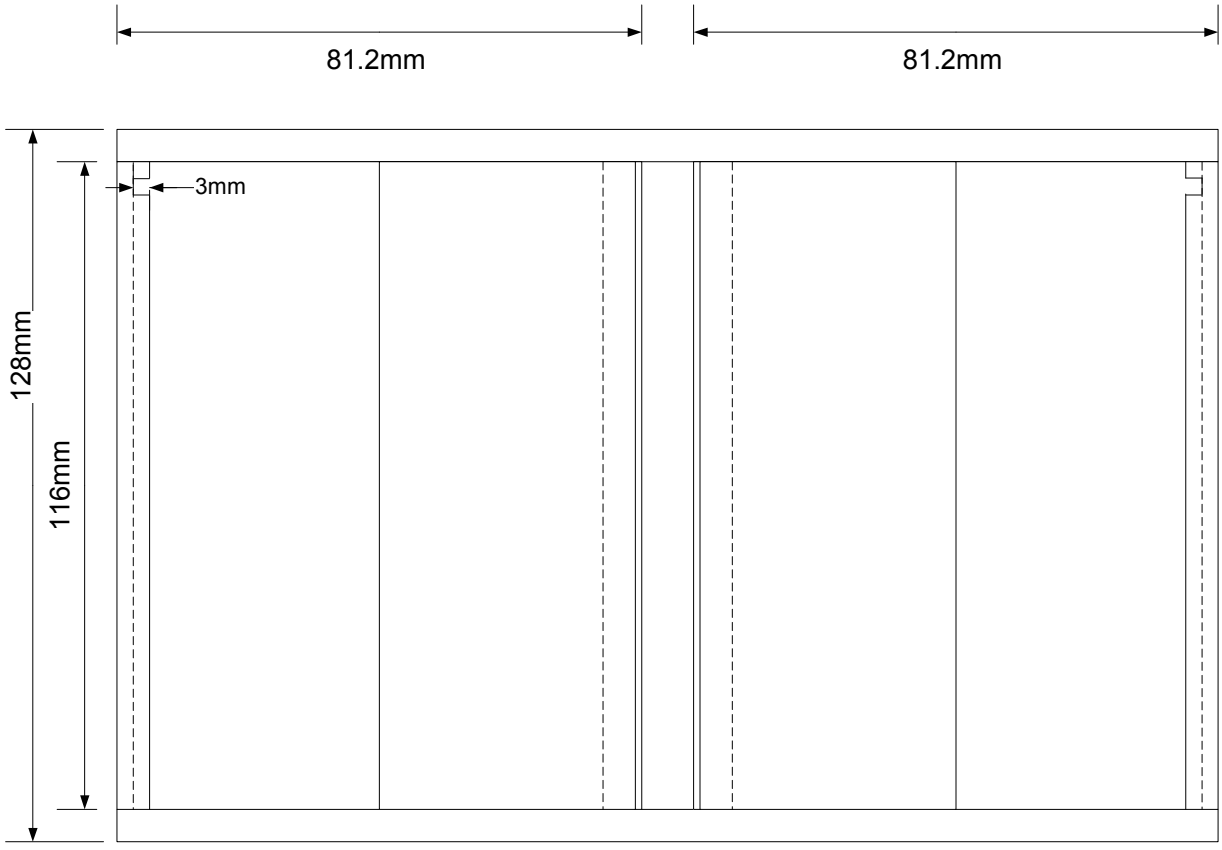

Figure 29: Top view drawings of the costume made gel box, with opening window for placing the sensors.

Appendix B

B.1 Work done on Improving p^+ layer of a-Si:H *pin* structures

B.1 Introduction

Nanocrystalline silicon (nc-Si:H) is a two phase material consisting of nano-crystallites embedded within an amorphous matrix and has gained considerable interest over the years as a low cost alternative in applications such as Thin Film Transistors (TFT), image detectors and solar cells. The most common a-Si:H photo detector is pin (a stack of p^+ doped a-Si:H + Intrinsic a-Si:H + n^+ doped a-Si:H) mainly because the depletion width thickness in the intrinsic layer can be tailored to optimize quantum efficiency of detection. The intrinsic layer sandwiched between the two doped layer is due to high defect density in doped layer in amorphous silicon detectors.

p and n layers create built-in voltage, and will not contribute to charge collection. All the charge collections take place in the intrinsic layer. Therefore it is crucial that the photons get absorbed in the intrinsic layer and not the p layer; in other words ideally the p layer should only act as a transparent window to the incoming light that assists in the creation of the built in voltage. Table 7 summarizes absorption coefficient and relative penetration length of some wavelengths. The penetration length is the distance photon travel before getting absorbed.

Table 7: Absorption coefficient and penetration length of different wavelength for a-Si:H.

λ(nm)	α_{si} (cm^{-1})	P layer(nm)	I layer(nm)	N Layer(nm)
190	$2x10^6$	5	-	-
300	$7.5x10^5$	5	9	-
375	$4x10^5$	5	30	-
450	$2.1x10^5$	5	30	40
600	$3.1x10^4$	5	30	100+

For short wavelength detection a very thin p layer with low defect density is required. Not only the p layer is important in the performance of the detector but also the p/i interface region has a strong influence on the electrical characteristics and stability of the device. This interface plays an important role on the internal electrical field distribution due to localized states in the interface that can acts as recombination centers and trap charges[27], [28]**.** Therefore any improvement in the thin p layer would enhance the responsivity of the device in the short wavelengths.

Combining advantages of both c-Si and a-Si:H (i.e., low production costs, better stability, improved charge mobility from the more ordered structure than a-Si:H). p^+ hydrogenated microcrystalline or nanocrystalline silicon (p^+ μc- or nc-Si:H) offers advantages over amorphous p^+ window layers. Compared to p^+ a-Si:H, the much higher electrical conductivity, resulting from a higher carrier mobility and doping efficiency, and the much lower light-induced degradation of p^+ μc- or nc-Si:H, reduces the series resistance, increases the built-in potential and improves the stability . p^+ μc- and nc-Si:H also have lower optical absorption in the UV-Visible-Near Infrared (UV-Vis-NIR) region compared to p^+ a-Si:H [27], and [28].

B.2 Experimental results and Discussions

A lower substrate temperature, T_{sub}, effectively reduces the mobility of hydrogen atoms, which are largely responsible for passivating dangling bonds for defect reduction. A higher defect density, or lower level of crystallinity, is normally found in low-temperature samples. Samples were deposited using a conventional PECVD system at T_{sub} of 150 °C. Thin films were deposited at different RF power density (83 mW/cm^2 – 413 mW/cm^2) and total chamber pressure (900 mTorr to 1900 mTorr). Source gases used were a mixture of hydrogen (H_2), silane (SiH_4) and diborane (B_2H_6). A hydrogen dilution ratio of $[H_2]/[SiH_4 + B_2H_6] \sim 200$ was selected for all p^+ nc-Si:H samples. The fixed deposition conditions for all our four samples are shown in

Table 8.

Table 8: Fixed deposition conditions for all the four p^+ nc-Si:H samples.

Deposition T	150°C
SiH_4 Flow Rate	1 Sccm
B_2H_6 Flow Rate	0.8 Sccm
H_2 Flow Rate	200 Sccm
Deposition Time	30 Minutes

Table 9, shows the sample number with the corresponding power and pressure chosen; each sample was deposited with the power of the associated column and the pressure of the associated row. For example, sample #1 was deposited with power of 10W and pressure of 0.9Torr.

Table 9: Deposition conditions (RF power, RF power density and total chamber pressure) for p^+ nc-Si:H samples and their respective sample names.

		RF Power [W] (RF Power Density [mW/cm^2])		
		10 (82.6)	30 (247.9)	50 (413.2)
Total Chamber Pressure [mTorr]	900	Sample #1		Sample #5
	1400		Sample #3	
	1900	Sample #2		Sample #4

Sample preparation

In order to characterize the crystallization in a very thin p layer, the films were lifted off from a sacrificing amorphous silicon nitride layer on top of the silicon substrate with diluted HF solution. The etching process had phosphoric acid and fluoric acid with ratio of 50:1, and it took almost one and half a day before the films could be fished out of the sample. Through a fishing process the films were fetched out of acid and placed in DI water and then placed in the carbon TEM grids, where they were left to dry out before using them in a TEM.

Transmission Electron Microscopy (TEM)

The bright-field (BF) images are shown from Figure 30 (a) to (d). The inset on each figure corresponds to the diffraction pattern of each sample. BF images were taken at a magnification of 70k with the Hitachi 8100 STEM and 200k times with the Tecnai 20 STEM. Diffraction patterns taken using the Hitachi 8100 STEM were adjusted such that the three brightest rings are shown.

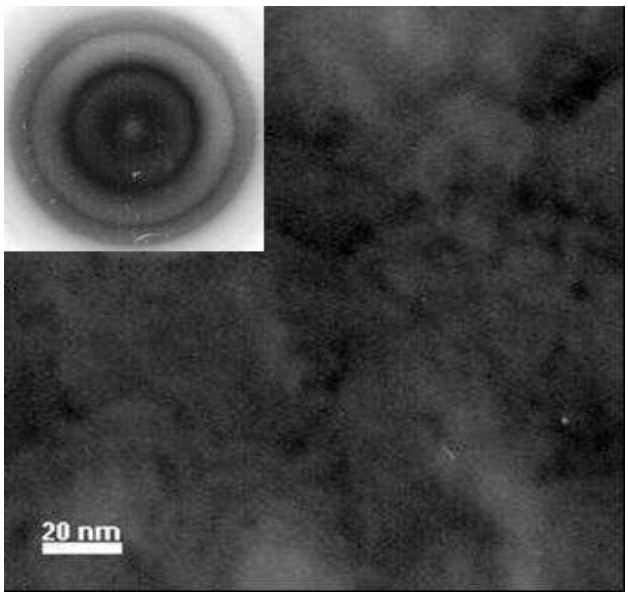

(a)

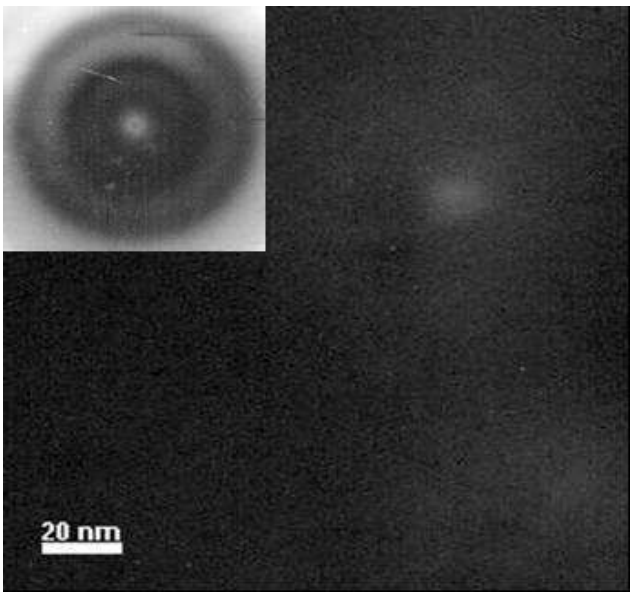

(b)

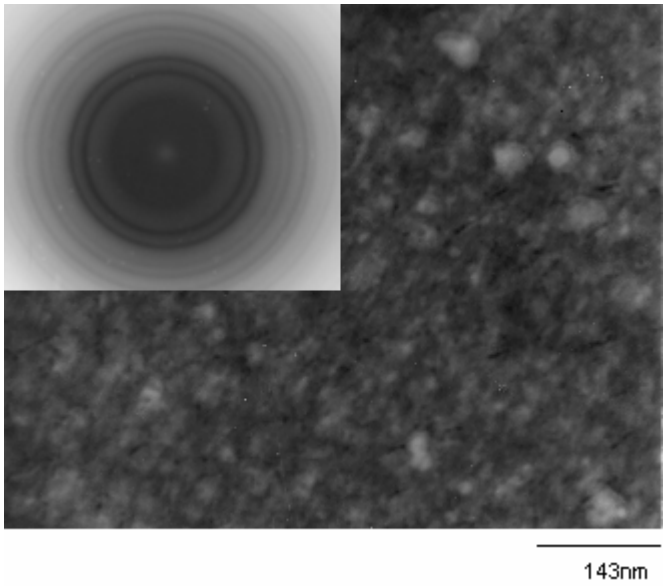

(C)

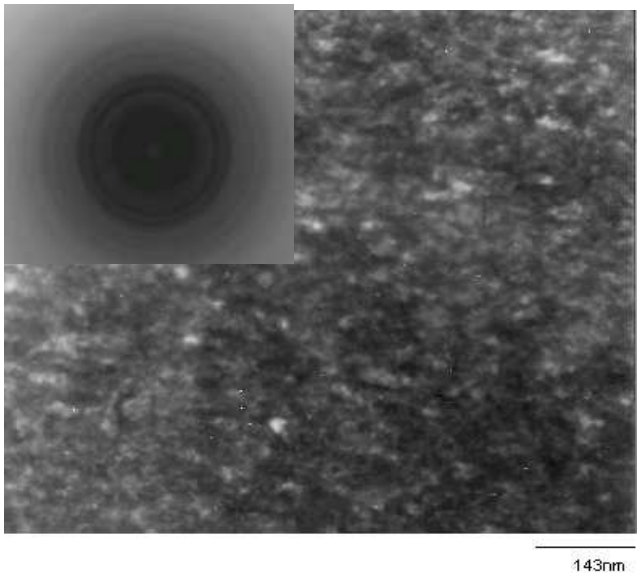

(d)

Figure 30: BF images and selected aperture (SA) diffraction patterns (DP) for samples deposited at 150 °C. (a) Sample #1, (b) Sample #2, (c) Sample #3, and (d) Sample #4.

Results and analysis from TEM measurements

From the BF images that were taken from the samples at 70Kx magnification, Figure 30, sample #1 and #2 showed some signs of nanocrystallinity, but the nanocrystals are very widely spread in the amorphous matrix. Also by looking at the DP of these two samples the thickness of the DP rings are large meanings that the grain size is very small. Between these two samples both the DP and the BF image shows more sign of nanocrystallinity for sample #1 than sample #2, and the only difference between the two is their pressure. This can be due to the fact that at higher pressure the rate of deposition is slightly higher and this would make the film grow faster which means more amorphous than nanocrystalline.

Both samples #3 and #4 showed nanocrystallinity with larger grain sizes, the small Si nanocrystals were embedded in hydrogenated amorphous silicon matrix. The separated bright dots correspond to nanocrystalline particles, most of the particles are ranging from 10-20 nm. The difference in samples #3 and #4 is that in sample #4, several large white dots are the cluster

of 3 to 4 neighboring crystals particles. Also the number of nanocrystalls in sample #4 is slightly more than in sample #3. From DP data the width of the diffraction rings would provide us with the grain size for the samples and can be used as an inverse measure of the grain size; for example thinner rings correspond to larger grain sizes and thicker rings correspond to finer ones. Comparing the width of the rings in DP of the samples, the width of the rings for samples #1 and #2 which were both deposited at 10W power, is much thicker than samples #3 and #4; confirming that the grain sizes in samples #1 and #2 are very small. This can also mean that the nano-crystals made in the hydrogenated amorphous silicon matrix are very few and far away from each other, and therefore the samples are more amorphous than nano-crystalline. Comparing samples #3 and #4 the width of the rings in sample #4 is slightly narrower than sample #3; this confirms the result from the bright field images that in sample #4 the cluster of 3 to 4 neighboring crystals particles makes the larger grain size and the number of these clusters are slightly higher than sample #3. High magnification images obtained for samples #4 is shown in

Figure 31. The purpose of this study is to confirm the nanocrystallinity and the orientation of the individual grains according to their lattice fringes. The grain sizes of sample #4 were estimated from these images, on average ~10 nm. The spacing between the lattice fringes of the selected grains in

Figure 31 was estimated to range from 2.85 Å to 3.25 Å. The average lattice spacing was therefore 2.99 Å. An average *d* spacing of 2.99 Å is closest to the *d* spacing of the Si (111) plane having a value of 3.13 Å. As a result, the <111> orientation in each grain is perpendicular to each set of fringes. Since the fringes are randomly oriented, the TEM shows a polycrystalline or nanocrystalline microstructure that is randomly oriented consistent with the SAD patterns.

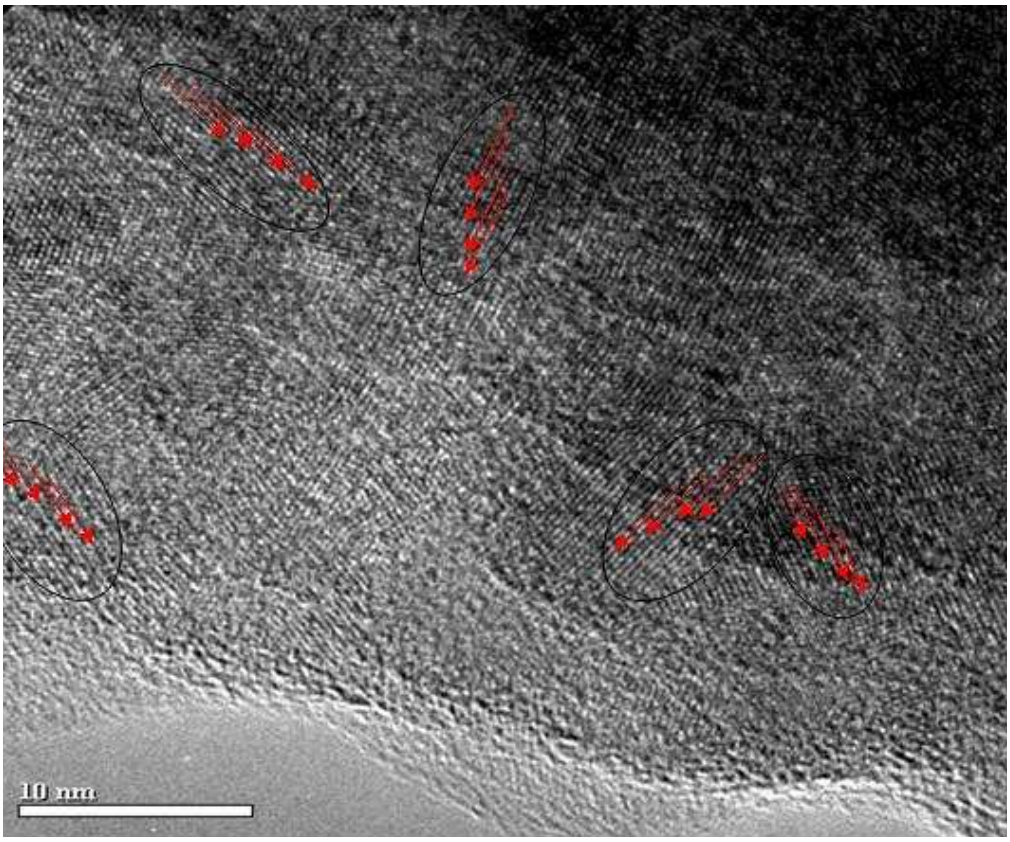

Figure 31.High magnification TEM image for Sample #4.

In all the DP figures, the first and second rings in the diffraction pattern are the darkest rings, so they should correspond to the most influential plane. For samples #3 and #4 the third ring is also clear, but for samples #1 and #2 the third ring is not as clear.

From the following equations, if the ratio between the radiuses of the rings (R) are taken and compared with [29], from the selection rules for cubic diamond crystal structures, these ratios for samples #3 and #4 agrees with hkl of (111) and (220), and (311), but for samples #1 and #2, since only the first two rings are clear the ratio agrees with planes (111), and (220).

$$\frac{R}{L}=\frac{\lambda}{d}, Rd=\lambda L \Rightarrow R_1 d_1 = R_2 d_2 = ...$$

$$Where \lambda (\ for V = 200KV) = \frac{h}{\sqrt{2m_e E}} \equiv 0.0025nm$$

$$\frac{1}{d^2}=\frac{h^2+l^2+k^2}{a^2} \Rightarrow \frac{d_1^2}{d_2^2}=\frac{h_2{}^2+l_2{}^2+k_2{}^2}{h_1{}^2+l_1{}^2+k_1{}^2}$$

Where L in the first equation is the camera constant; therefore we can also calculate the corresponding d for each ring.

Samples #3 and #4

Rings	Diameter(mm)	Radius(mm)	d (A)	ICSD d_{Si}	$\frac{d_n^2}{d_{n+1}^2}$	$\frac{h_{n+1}{}^2+l_{n+1}{}^2+k_{n+1}{}^2}{h_n{}^2+l_n{}^2+k_n{}^2}$	$h^2+l^2+k^2$	hkl
R_1	13.1	6.55	3.1	3.1352			3	111
R_2	21.2	10.6	1.9	1.9199	2.6	2.67	8	220
R_3	25.5	12.8	1.6	1.6373	1.4	1.38	11	311

Samples #1 and #2

Rings	Diameter(mm)	Radius(mm)	d (A)	ICSD d_{Si}	$\frac{d_n^2}{d_{n+1}^2}$	$\frac{h_{n+1}{}^2+l_{n+1}{}^2+k_{n+1}{}^2}{h_n{}^2+l_n{}^2+k_n{}^2}$	$h^2+l^2+k^2$	hkl
R_1	12.5	6.25	3.2	3.1352			3	111
R_2	21.5	10.8	1.9	1.9199	2.9	2.67	8	220

The same deposition condition as for sample #4 were used to fabricate very thin p^+ layers about 10 nm; the TEM experiments on the obtained films for DP results indicated no ordered structure hence showed only amorphous structures; which agrees with previous studies for μc and nc-Si:H film growth, where studies relating dark conductivity (σ_d) to film thickness (t) have shown that σ_d has an increase of several orders of magnitude in the 20 nm – 30 nm region, indicating the presence of a hydrogen-rich porous amorphous incubation phase prior to crystalline growth [30], and [31].

Therefore we conclude that deposition conditions used for highly crystalline, thick p^+ samples may not yield equally promising properties if used for thin samples which also agrees with [32], since initial micro- and nano-crystalline growth is known for being extremely inhomogeneous in the direction perpendicular to the substrate surface [33].